

Section 5

Development of and studies with regional and smaller-scale atmospheric models, regional ensemble, monthly and seasonal forecasting

Enhancement of Computational Stability in the Mesoscale Model of the Japan Meteorological Agency

Kohei Aranami

Numerical Prediction Division, Japan Meteorological Agency

1-3-4, Otemachi, Chiyoda-ku, Tokyo 100-8211, Japan

E-mail: aranami@met.kishou.go.jp

1 Introduction

The Japan Meteorological Agency (JMA) has operated a mesoscale numerical weather prediction system (MSM) for disaster prevention and aviation forecasting since March 2001. A non-hydrostatic model (JMA-NHM; Saito et al., 2006) was introduced in September 2004, and has been in operational use since then. The horizontal resolution was enhanced from 10 km to 5 km in March 2006, and the forecast time was extended from 15 to 33 hours in May 2007.

During the summer of 2007, the MSM terminated abnormally up three times due to computational instability caused by small-scale storms associated with tropical depressions.

2 Characteristics of the abnormally terminated cases

Figure 1 shows the case initialized at 09 UTC on 7th August 2007. Very intense precipitation (over 170 mm/hour, not shown) was calculated around Typhoon Pubuk (T0706), which was approaching the island of Taiwan in this case. Figure 1 (b) shows a cross section of the rain. An abnormally jagged rain distribution with a strong vertical wind speed was calculated. The common characteristics of the abnormally terminated cases were as follows: (i) instability occurred around a tropical depression; (ii) abnormally jagged distributions of rain (and graupel) were seen around the regions of instability; (iii) topography was not necessarily a factor, as instability occurred around 24 °N 137 °E over the sea.

3 Modifications against computational instability

Figure 2 shows a cross section of the mixing ratio of rain for another abnormally terminated case. Jagged distribution was also seen here. This abnormal pattern was considered to be the result of an issue in dealing with the vertical advection and sedimentation of rain and graupel. Figure 3 shows the same data as Figure 2 but for an experiment in which sedimentation flux time integration was made in the adjustment process, instead of the tendency included in cloud microphysics. This approach appears to be effective in removing the jagged distribution, but the precipitation histogram changes and the vertical wind speed remains strong. Another approach should therefore be considered.

To prevent serious deterioration of forecasting by the model, the modifications outlined below were implemented, and were mainly applied for columns with strong vertical wind speed. (1) Modification of the Target Moisture Diffusion (TMD; Saito and Ishida, 2004): TMD was changed to apply it to all grid points in vertical columns, while the original scheme was designed to apply it to grid points. The threshold value of TMD was also changed from the vertical speed of the z^* coordinate to that of hybrid coordinates. TMD was changed so that it is also activated for columns adjacent to those where it is triggered in order to improve water vapor conservation. (2) Modification of the Box-Lagrangian scheme

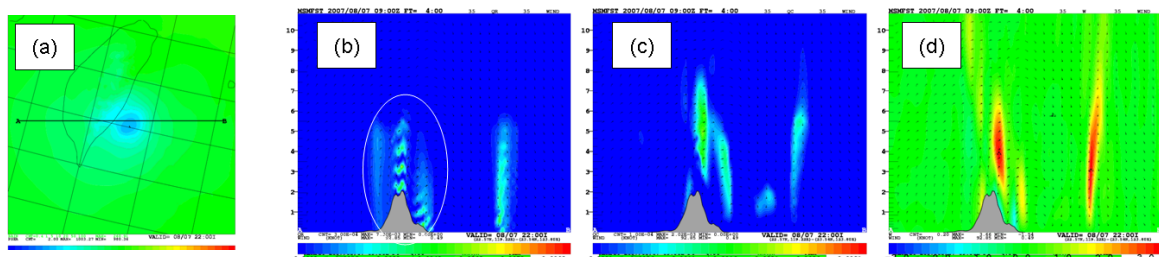


Figure 1: (a) Horizontal distribution of sea level pressure around Taiwan island at the forecast time of 4 hour for the case of 7th August 2007. (b) Cross section of mixing ratio of rain along with line AB. (c) Cross section of mixing ratio of cloud water. (d) Cross section of the vertical wind speed.

(BL; Kato, 1998): The correction method for the tendencies of the BL scheme was designed to avoid negative values of water substances after each cycle of time integration in consideration of the original value (value at $t - \Delta t$), the tendency from cloud microphysics and the BL scheme. The BL scheme was changed to consider the tendency from advection and diffusion in addition to the above tendencies. (3) Change in the vertical advection scheme for rain and graupel: To avoid jagged distribution, a first-order upwind advection scheme was applied for rain and graupel with columns where the maximum vertical wind speed exceeds 6 m/s. (4) Modification of the Kain-Fritsch scheme (K-F, Kain and Fritsch, 1990): The following three changes were introduced for columns where the maximum vertical wind speed exceeds 3 m/s: (i) The removal ratio of CAPE (Convective Available Potential Energy) under the K-F scheme was changed from 85% to 100%. (ii) Limitation of the lifetime of deep convection was abolished. (iii) The tendencies already applied were reset and recalculated. (5) Increase of nonlinear damping strength (Nakamura, 1978): The time constant of nonlinear damping for all prognostic variables was changed from 1,200 seconds to 600 seconds for effective reduction of the vertical wind speed.

By applying (1) - (5), the jagged distribution shown in Figure 2(b) was alleviated significantly. The result was intermediate between Figure 2(b) and Figure 3(b).

4 Results of a longer period experiment and Conclusion

It was confirmed that all the abnormally terminated cases in 2007 were integrated stably when the modifications described in this article were applied. The statistical verifications for a 2-week period in summer and a 1-week period in winter confirm that the model performance is neutral before and after the modifications. These modifications were implemented to the operational model in September 2008.

Thus various kinds of modifications to avoid the computational instability have been implemented to the MSM at JMA, without deteriorating the model accuracy. Yet the treatments implemented this time are tentative. To solve the computational instability problem at bottom, we need to scrutinize the fundamental part of model, which may be the interaction of dynamical and physical processes.

References

- [1] Nakamura, H., 1978: Dynamical effects of mountains on the general circulation of the atmosphere : 1. Development of finite-difference schemes suitable for incorporating mountains. *J. Meteor. Soc. Japan*, **56**, 317-339.
- [2] Kato, T., 1995: A box-Lagrangian rain-drop scheme. *J. Meteor. Soc. Japan*, **73**, 241-245.
- [3] Kain, J. S. and J. M. Fritsch, 1990: A one-dimensional entraining/detraining plume model and its application in convective parameterization. *J. Atmos. Sci.*, **47**, 2784-2802.
- [4] Saito, K., T. Fujita, Y. Yamada, J. Ishida, Y. Kumagai, K. Aranami, S. Ohmori, R. Nagasawa, S. Kumagai, C. Muroi, T. Kato, H. Eito and Y. Yamazaki 2006: The operational JMA Non-hydrostatic Mesoscale Model. *Mon. Wea. Rev.*, **134**, 1266-1298.

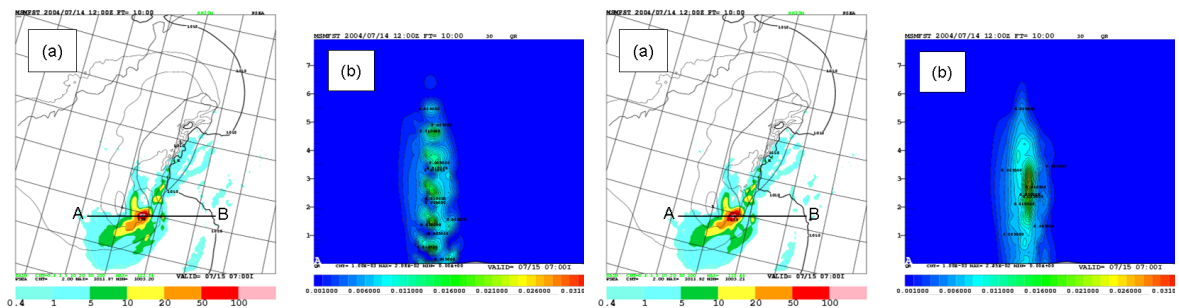


Figure 2: (a) 1 hour accumulated precipitation and sea level pressure at forecast time of 10 hours of the case of 12UTC 14 July 2004 initial. (b) Vertical cross-section of rain along the line AB in the left panel. Figure 3: Same as Figure 2 but for the experiment with adjustment time integration of sedimentation flux.

Short-range numerical forecast system supporting the field experiment of cloud seeding

Akihiro Hashimoto, Teruyuki Kato, and Masataka Murakami

Meteorological Research Institute, Japan Meteorological Agency

1. Introduction

Closely-designed short-range numerical forecast system with a high-resolution model in a particular area targeted in a special field observation provides the information on three dimensional distributions of temperature, humidity, wind speed and direction, and liquid and solid hydrometeors which is useful for the observational director planning the experiment in the following day. Such the information also supports the in-situ operators to foresee the behavior of atmosphere and to correctly recognize the environmental condition. The special forecast system involved into the field observation can yield the interactive communication between the observational operators and model developers so as to further improve the numerical model.

In the Meteorological Research Institute (MRI), Japan Meteorological Agency (JMA), a research project is now on progress to examine the feasibility of cloud seeding technique enhancing the snowfall in Echigo Mountains which is the main water reservoir for the Tokyo metropolitan area. We have established a short-range numerical forecast system to specially support an airborne cloud seeding experiment in the project. In this system, we conduct the successive simulations using a three dimensional cloud seeding model with the horizontal resolution of 1 km (1km-NHM). The design of the system and its efficacy will be reported hereafter.

2. Design of a special forecast system supporting the field experiment

a. Cloud seeding model

We have developed a cloud seeding model based on the Japan Meteorological Agency NonHydrostatic Model (JMA-NHM; Saito *et al.*, 2006). The JMA-NHM has five categories of liquid and solid water substances: cloud water, rain, cloud ice, snow, and graupel, as described in Ikawa and Saito (1991). In this study, a two-moment bulk parameterization scheme, which prognoses both the mixing ratio and number concentration, is applied to the categories of solid hydrometeor, while one-moment scheme, which prognoses only mixing ratio, is applied to those of liquid hydrometeor. In addition to the original model specifications, a new module is implemented so as to simulate the airborne cloud seeding with dry ice pellets, introducing the processes of deposition and fall out of dry ice pellets, and artificial ice nucleation. The module also has the other functions to simulate the cloud seeding using liquid carbon dioxide and silver iodide not only from an aircraft but also from the ground-based generators.

Corresponding author: Akihiro Hashimoto, Meteorological Research Institute, 1-1 Nagamine, Tsukuba, 305-0052, Japan. E-mail: ahashimo@mri-jma.go.jp

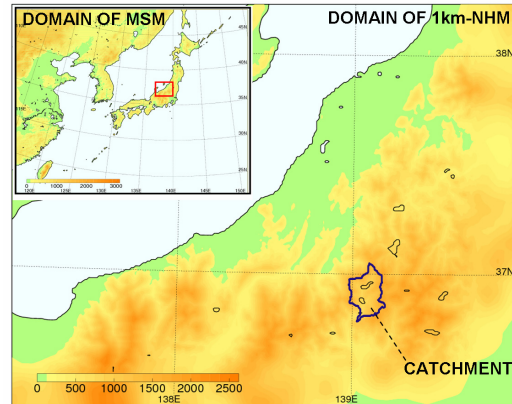


Fig. 1 Domains for the MSM and 1km-NHM.

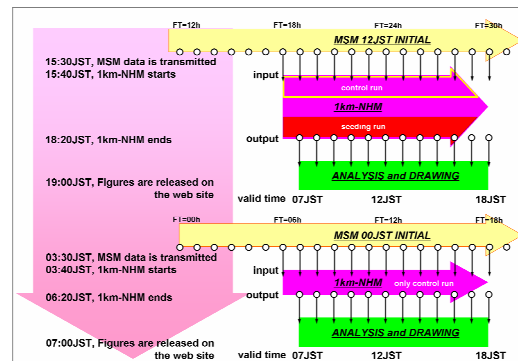


Fig. 2 The sequence of simulation and data handling.

b. Procedure of successive simulations

The numerical forecast data of the JMA mesoscale model with a 5-km horizontal resolution (MSM) is specially forwarded from the JMA headquarter for the project. The 1km-NHM is embedded into the MSM domain, as shown in Fig. 1. Figure 2 shows the sequence of simulation and data handling. The 12-hours control (no seeding) forecast for daytime (06-18 JST, JST = UTC + 9 hours) is performed twice a day using the MSM forecasts with the initial time of 00 JST and 12 JST as the initial and boundary conditions. The simulation for each forecast day finishes around 06 JST at that day and around 18 JST in the previous day, since those simulations are preferentially executed in the super computer system of the MRI. In an hour after then, the final output in the form of figures is presented on the web site for the field experiment.

For the forecast involving cloud seeding, we have made up

an optimally positioning scheme that empirically estimates the seeding position maximizing the seeding effect on the surface snowfall in a targeted dam catchment for a given atmospheric condition. The scheme is established based on the sensitivity experiments in which cloud seeding simulations are conducted changing the distance from the dam site to the seeding position along the environmental wind direction for each of 14 different cases to find the optimal seeding position (Hashimoto *et al.*, 2008a). After the control forecast for the next day finished around 18 JST, the seeding forecast is conducted with the same initial and boundary conditions. The seeding rate of dry ice pellets is set to 3 kg min^{-1} . The flight speed of seeding airplane is assumed to be 100 ms^{-1} in the model. The cloud seeding starts one-hour after the launch of simulation and continues until the end (07-18 JST).

3. Available information

a. Basic information

The information on the patterns of pressure, temperature, water vapor, wind and surface precipitation is presented twice a day on the web site. The information in the evening is useful to make a plan for the experiment in the following day, and that in the morning will be a help for a decision on the operation at that day.

For the cloud seeding, it is the most important to know whether the super-cooled cloud appears upstream the targeted area. In addition, it is a clue for the evaluation of seedability (how preferable the atmospheric situation is for the cloud seeding) to know how much glaciated the clouds to be seeded are in the natural. For those purposes, the hourly distributions of liquid and solid hydrometeors, temperature, and humidity in the vicinity of the seeding area are provided, based on the control forecast.

b. Special information for cloud seeding operation

Hashimoto *et al.* (2008b) found the relationship between the seedability and meteorological parameters from the results of the hindcast experiment through the winter seasons of 2005/06 and 2006/07. This relationship enables us to provide the guidance on the seedability for the cloud seeding operators, based on the control forecast. In addition to the seedability, the optimal seeding position which is determined with the optimally positioning scheme is included in the guidance, as shown in Fig. 3.

The predicted seeding effect on the surface precipitation is also presented on the web site by subtracting the result of the control forecast from that of the seeding one, as shown in Fig. 4.

4. Discussions and summary

The short-range numerical forecast system with a three dimensional cloud seeding model is able to provide the useful information for the cloud seeding experiment. The optimally positioning scheme applied in the present study still has a room open to discussion in terms of the accuracy of determined position, as pointed out in Hashimoto *et al.* (2008a). The authors plan to further improve the system so as to apply into the future operational project.

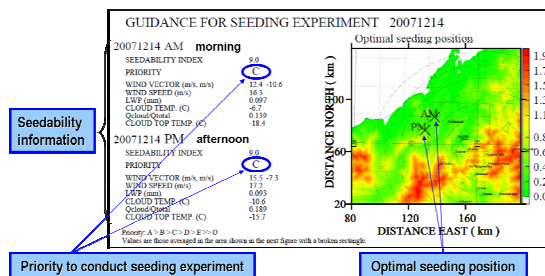


Fig. 3 Guidance on seedability, provided on 14th December, 2007 in the IOP.

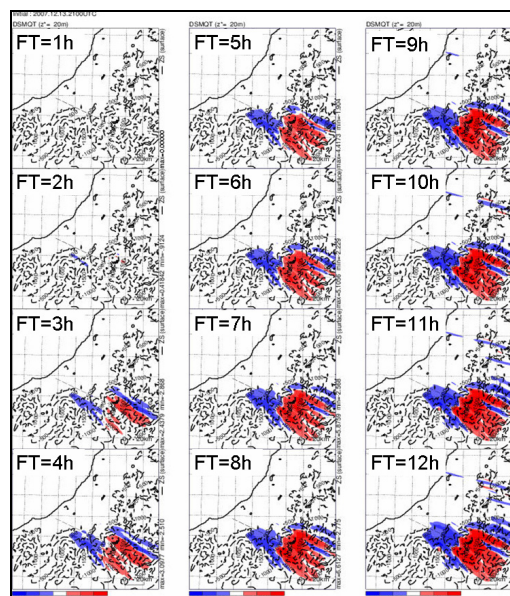


Fig. 4 Accumulated effect of seeding on the surface precipitation.

References

Hashimoto, A., T. Kato, S. Hayashi, and M. Murakami, 2008a: Numerical experiment on the sensitivity of precipitation enhancement to cloud seeding position for the winter orographic cloud in Japan. *Research Activities in Atmospheric and Oceanic Modelling/WMO*, 38, 5-09 – 5-10.

Hashimoto, A., T. Kato, S. Hayashi, and M. Murakami, 2008b: Seedability assessment for winter orographic snow clouds over the Echigo Mountains, *SOLA*, 4, 069-072.

Ikawa, M. and K. Saito, 1991: Description of a nonhydrostatic model developed at the Forecast Research Department of the MRI. *Tech. Rep. MRI*, 28, 238pp.

Saito, K., T. Fujita, Y. Yamada, J. Ishida, Y. Kumagai, K. Aranami, S. Ohmori, R. Nagasawa, S. Kumagai, C. Muroi, T. Kato, H. Eito, Y. Yamazaki, 2006: The operational JMA nonhydrostatic mesoscale model. *Mon. Wea. Rev.*, 134, 1266–1298.

Research on fuzzy verification in high-resolution precipitation forecasts

Yasutaka Ikuta¹, Yuki Honda²

Numerical Prediction Division, Japan Meteorological Agency,
1-3-4, Otemachi, Chiyoda-ku, Tokyo 100-8122, Japan

A high-resolution local forecast model (LFM) with a grid spacing of 2 km is being developed by the Japan Meteorological Agency. The LFM is nested into the operational mesoscale model (MSM), which is another limited-area model with a grid spacing of 5km. To compare the performance of the LFM with that of the MSM, verification of quantitative precipitation forecasts (QPFs) is required. However, traditional verification methods such as bias score and threat score are not adequate because these methods cannot handle forecast displacement error appropriately. This kind of issue regarding verification scores is often referred to as the ‘double penalty’ problem.

For the last several years, the verification for high-resolution model forecasts has been discussed enthusiastically in research fields, and several new verification techniques have been proposed. One of the main characteristics of these new techniques is the introduction of the concept of spatial scale into the verification. The new verification techniques tolerate the difference of the spatial structure pattern within the spatial scale, and are referred to as *spatial verification* methods. One of them is the fuzzy verification methods, which considers the precipitation of neighborhood grids. In this report, several fuzzy verification methods are tested to evaluate the QPFs of the LFM and the MSM.

We tested the following fuzzy verification methods: 1) Upscaling (Yates et al., 2006); 2) Fuzzy Logic (Damrath, 2004; Ebert, 2002); 3) Intensity Scale (Casati et al. 2004); 4) Fractions Skill Score (Roberts and Lean 2008). More fuzzy verification methods in addition to the ones given here are listed in Ebert (2008). We ascertained the characteristics of these methods as described below.

The upscaling method has the problem of providing no computed values for large spatial scales and high thresholds. Fuzzy logic, on other hand, gives uncertain scores for large spatial scales. As an example, in the perfect forecast of an idealized experiment, the ETS becomes a value other than 1. The Intensity scale skill score (ISS) can detect displacement error, but is insensitive to the frequency bias of forecasts. The Fractions Skill Score (FSS) provides a target skill giving a general criterion for a skillful forecast. This target skill is defined as half the value of the scores between a random forecast and a perfect forecast, and a poor forecast with typical displacement larger than twice as long as neighborhood length gives score under the target skill. In addition, the rates exceeding the target skill provide an estimate of the minimum useful scale, but this scale becomes useless in forecasts with large biases. The forecast frequency bias is represented by a conventional bias f_M/f_o , where f_o is the observed frequency and f_M is the model-forecast frequency. This conventional bias is equal to the bias score from a contingency table in the grid scale. If the neighborhood length covers the whole verification area, the FSS becomes $2f_o f_M / (f_o^2 + f_M^2)$. This skill score is called the *asymptotic fractions skill score* (AFSS). In particular, the AFSS of a no-bias forecast is equal to the value of 1.

We have reached the conclusion that upscaling and the fractions skill score are appropriate for verification of high-resolution QPFs. In particular, the FSS provides new information on displacement error as the target scale. The following discussion of a real case study is focused on the FSS approach. Figure 1 shows FSSs with two different spatial scales of QPFs of the MSM and the LFM for April 2008. Figure 2 shows a comparison with the averaged conventional bias of these values. In the grid scale (Fig. 1 (a)), the LFM had a lower value for the skill score and the over-target rate than the MSM at almost all thresholds, and the AFSS of the LFM was larger than that of the MSM for the 15 mm/3 h and the 20 mm/3 h thresholds. For thresholds lower than 10 mm/3 h the AFSS of the LFM was close to that of the MSM, when the LFM conventional bias was smaller than that of the MSM. In contrast, the frequency bias of the MSM shows a low value for high thresholds. Figure 1 (b) shows that, for a spatial scale of 80 km, the over-target rate of the LFM becomes similar to that of the MSM. Moreover, these LFM scores are larger than those of the MSM for the 15 mm/3 h, 20 mm/3 h and 30 mm/3 h thresholds.

In this study, the frequency of high-resolution forecasts was small for low thresholds and large for high thresholds. Moreover, for large thresholds, the FSS of low-resolution forecasts was lower than that of

¹ E-mail: ikuta@met.kishou.go.jp

² E-mail: honda.yuuki@met.kishou.go.jp

high-resolution forecasts. This FSS behavior could represent the characteristics of high-resolution precipitation forecasts which were usually underestimated as a result of displacement error. Figure 1 (b) shows that the increase in spatial scale gave LFM scores that were larger than those of the MSM at the 15 mm/3 h, 20 mm/3 h and 30 mm/3 h thresholds. These results indicate that introducing an adequate spatial scale in precipitation verification successfully relaxes the requirement for perfect matching. Accordingly, it can be seen that the FSS represents an appropriate approach for verification of the high-resolution model.

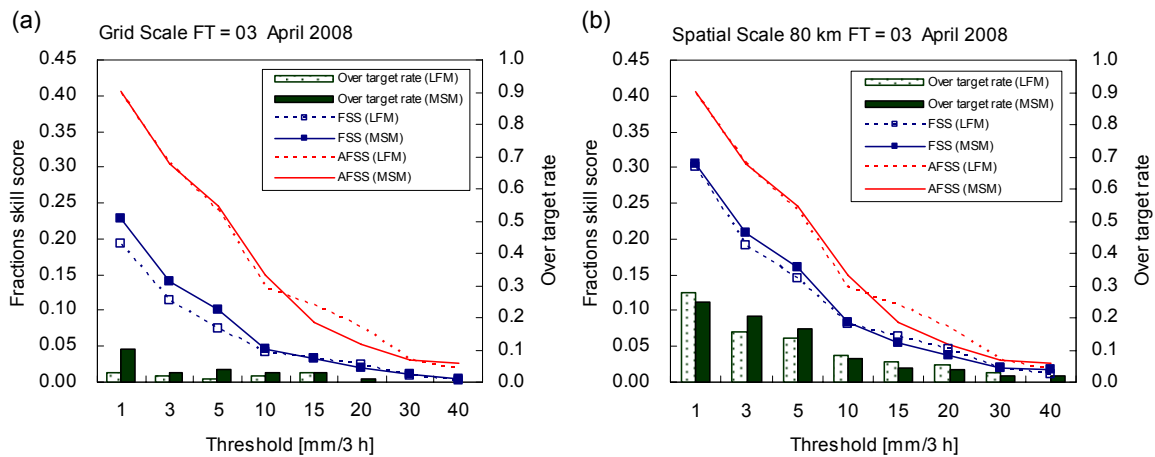


Figure 1. Fractions skill score (line plots with symbols), asymptotic fractions skill score (line plots) and rate of over-target skill (bar charts) are shown as a function of threshold and three hour accumulation. Each score was calculated in (a) the grid scale, and (b) the spatial scale of 80 km.

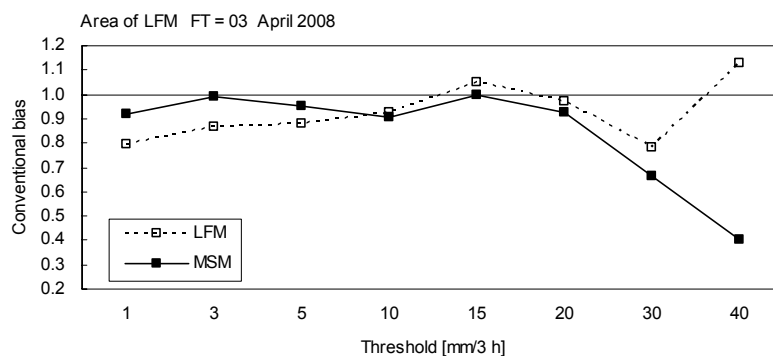


Figure 2. Conventional bias $\overline{f_M/f_o}$ (line plots with symbols) is shown as a function of threshold for April 2008, where over-bars ($\overline{\quad}$) indicate the monthly average.

References

- Yates, E., S. Anquetin, V. Ducrocq, J.-D. Creutin, D. Ricard and K. Chancibault, 2006: Point and areal validation of forecast precipitation fields. *Meteorol. Appl.*, **13**, 1-20.
- Damrath U. 2004: Verification against precipitation observations of a high density network – what did we learn? In International Verification Methods Workshop, Montreal, 15–17 September 2004.
- Ebert EE. 2002: Fuzzy verification: giving partial credit to erroneous forecasts. In NCAR/FAA Verification Workshop: Making Verification More Meaningful, NCAR, Boulder, 30 July – 1 August 2002.
- Casati, B., Ross, D.B. Stephenson, 2004: A new intensity-scale approach for the verification of spatial precipitation forecasts. *Meteorol. Appl.*, **11**, 141-154.
- Roberts, N. M. and H. W. Lean, 2008: Scale-selective verification of rainfall accumulations from high resolution forecasts of convective events. *Mon. Wea. Rev.*, **136**, 78–97.
- Ebert EE, 2008: Fuzzy verification of high resolution gridded forecasts: A review and proposed framework. *Meteorol. Appl.*, **15**, 51–64.

Development of a New Dynamical Core for the Nonhydrostatic Model

Junichi Ishida, Chiashi Muroi, and Yuri Aikawa

Numerical Prediction Division, Japan Meteorological Agency

E-mail: j_ishida@naps.kishou.go.jp, cmuroi@naps.kishou.go.jp, aikawa@met.kishou.go.jp

1. Introduction

A new dynamical core for JMA's nonhydrostatic model is now under development for mesoscale numerical weather prediction. JMA presently operates the global spectral model (GSM) and a nonhydrostatic regional model (Mesoscale Model: MSM) within the current operational supercomputer system. The recent rapid increase in market share of scalar multi-core architecture machines and the spaghetti code of the current regional model have motivated us to renovate the model. This paper gives a brief outline of the new dynamical core of the revised nonhydrostatic model, called "ASUCA". The new version is intended for operation as a regional cloud-resolving model at JMA.

2. Outline of the new dynamical core

Flux-form fully compressible equations are applied as the governing equations for this model. The prognostic variables are ρu , ρv , ρw , $\rho\theta$ and ρ , where u , v and w are the components of wind velocity, θ is potential temperature and ρ is density. The equations are transformed using general coordinate transformations, which enable the new model to be extended to a global nonhydrostatic version. The only assumptions are that the transformed coordinates have flat lower boundaries regardless of topography and the axis of a transformed coordinate is parallel to the vector of gravity acceleration.

The finite volume method (FVM) is applied to the transformed equations. A structured quadrilateral grid is employed, which makes the data structure simple. A mass conservation equation is directly integrated using FVM and mass is conserved throughout the whole domain including lateral boundary inflow and outflow. No correction scheme is required for mass conservation. An accurate flux correction advection scheme is employed to avoid causing oscillations, and this scheme employs the flux limiter function proposed by Koren (1993). The correction scheme for conservation and avoidance of negative quantity can be simplified. These features reduce the computational cost and the amount of data communication required for numerical stability and conservative properties.

A third-order Runge-Kutta scheme (Wicker and Skamarock, 2002) is applied for time discretization. A split-explicit time integration scheme (Klemp and Wilhelmson, 1978) is used to avoid small time steps caused by sound waves. Pressure gradient terms

and divergence terms are treated in the shorter time step, and other dynamical and physical processes are evaluated in the longer time step. In the short time step, horizontal velocities are integrated first in an explicit manner, and vertical velocity and density are solved implicitly.

3. Software design

The code of this new model is designed for parallel architecture machines including PC clusters. Fortran90 and MPI are used in the code, and OpenMP directives are inserted into it for multi-thread environments. Since the latency time of the data communication is not small, the code is also designed to reduce the number of calling of MPI subroutines. Three-dimensional arrays in space are stored sequentially in the order of z (k), x (i) and y (j). To avoid spaghetti code, style and coding rules are also prescribed.

4. Summary and future plan

We are currently testing the new dynamical core through a range of idealized experiments. We have also incorporated a number of simple physical processes, and are implementing trial runs of the model using real data.

There is also a need to develop more sophisticated software design. Since the source code for physical processes will be shared between the new model and the current nonhydrostatic regional model, it is necessary to develop efficient methods of code sharing.

The dynamics core also needs to be more sophisticated. For example, if water substances with a fast fall velocity (such as rain or graupel) are used as prognostic variables, another scheme to treat advection is necessary. We plan to introduce the piecewise rational method (Xiao and Peng, 2004) for this purpose.

References

- Klemp, J. B., and R. B. Wilhelmson, 1978: The simulation of three-dimensional convective storm dynamics. *J. Atmos. Sci.*, 35, 1070-1096.
- Koren, B., 1993: A Robust Upwind Discretization Method for Advection, Diffusion and Source Terms. CWI Report NM-R9308.
- Wicker, L. J., and W. C. Skamarock, 2002: Time-splitting methods for elastic models using forward time schemes. *Mon. Wea. Rev.*, 130, 2088–2097.
- Xiao, F., and X. Peng, 2004: A convexity preserving scheme for conservative advection transport. *J. Comp. Phys.*, 198, 389-402.

Numerical Experiments of Myanmar Cyclone Nargis

Tohru KURODA, Kazuo SAITO, Masaru KUNII and Nadao KOHNO

Meteorological Research Institute, Tsukuba, Ibaraki 305-0052, Japan; tkuroda@mri-jma.go.jp

On 27 April 2008 cyclone Nargis formed in the Bay of Bengal and made landfall on 2 May in southwestern part of Myanmar. The cyclone and the associated storm surge caused heavy human damages. If an appropriate warning was issued about 2 days before the landfall, the number of casualties might have been reduced drastically. In order to show the performance of the downscale NWP using NHM and JMA data, we performed a forecast experiment of Nargis. We also simulated the storm surge with the Princeton Ocean Model (POM) using the NHM forecast data.

We conduct a regional forecast with NHM, using the JMA global analysis (horizontal resolution is about 20 km) as the initial condition and the GSM global forecast (horizontal resolution is about 50 km and valid time is every 6 hours) as the boundary condition. We also use the JMA global land surface analysis and JMA global SST analysis. NHM is executed with a horizontal resolution of 10 km for a square region of 3400 km around the Bay of Bengal (Fig. 1).

Considering the lead time for warning, the initial time is set to 12 UTC 30 April, 2008. In the JMA analysis, Nargis was expressed as a weak depression of 999 hPa in the center of the Bay of Bengal, and its position was deviated eastwardly about 0.7 degree in longitude compared with the best track (Fig. 2). After 42 hour (06 UTC 2 May), the depression developed to a 972 hPa cyclone and reached southwestern part of Myanmar in the NHM forecast (Fig. 1, right). Although this central pressure is weaker than estimated intensity of Nargis (Category 4), the value is much deeper than the GSM forecast (994 hPa; Fig. 1, left).

Figure 2 compares tracks of Nargis predicted by NHM and GSM with the best track. Cyclone landfall time in the NHM forecast was 6 hours earlier than the best track, and this is mainly attributable to the 0.7 degree positional lag in the initial condition mentioned above. In the GSM forecast, predicted course of Nargis is closer to the best track than NHM, but the positional lag at FT=42 is larger than NHM because the timing of landfall is earlier than NHM. Although the landfall point of NHM forecast was deviated about 100 km northwardly than the best track, NHM predicted the strong winds which covered the southern part of Myanmar including the Irrawaddy and Yangon Deltas.

Using the NHM forecasted data (surface wind and pressure), we conducted a numerical simulation of the associated storm surge with POM. POM is a free surface ocean model

developed at Princeton University. The horizontal resolution is about 3.5 km and vertically 12 layers sigma coordinates are employed. The domain size is 451x391 which covers eastern part of the Bay of Bengal (broken rectangle in Fig. 1). In the simulation, the initial state is assumed to be static, and the astronomical tide and wind waves are not considered.

Figure 3 shows displacement of sea surface level simulated by POM at 00 UTC 2 May 2008 (FT=36). At this time, the center of the simulated Nargis is located off the west coast of southern Myanmar, and a rise of sea-level due to low pressure near cyclone center is seen as a circular contour. In the enlarged view, we can see that southerly sea surface current generated by surface wind flows into mouths of rivers in southern Myanmar (*e.g.*, Irrawaddy River and Yangon River).

Figure 4 indicates time sequence of surface (10 m) wind speed, wind direction and water displacement of sea surface level at the mouths of Irrawaddy River (16.10N, 95.07E) and Yangon River (16.57N, 96.27E). At points in these river mouths, water levels become highest at the times when the southerly winds are strongest. This correspondence between peaks of wind speed and water level suggests that surface current generated by wind is a major cause of water level rising in these areas. At 07 UTC (FT=43), displacement of sea surface level about 3.2 m is simulated at the Irrawaddy River point, which is roughly consistent with the reported magnitude of storm surge in southern Myanmar.

Result of a mesoscale ensemble forecast with NHM to consider uncertainties of initial and lateral boundary conditions is given by a separate study (Saito et al.; this volume). To further reduce errors of intensity and track forecast, data assimilation is a future subject.

Acknowledgement

This study is supported by the Asia S&T Strategic Cooperation Program (MEXT Special Coordination Funds for Promoting Science and Technology).

References

- K. Saito, T. Kuroda and M. Kunii, 2009: Ensemble Forecast Experiment of Cyclone Nargis. *CAS/JSC WGNE Research Activities in Atmospheric and Oceanic Modeling*. **39**. (this volume)

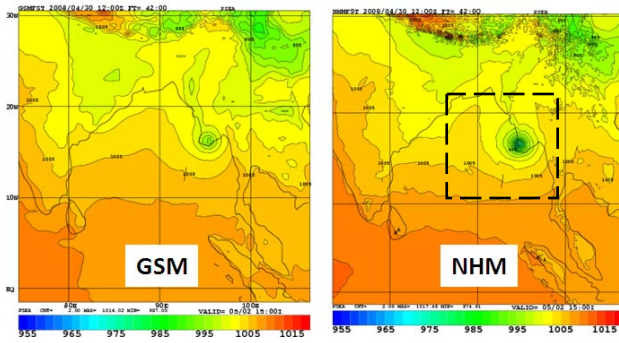


Fig. 1. Sea level pressure at 06 UTC 2 May 2008 (FT=42) predicted by GSM (left) and NHM (right). Figures show the domain of NHM and broken rectangle indicates the domain of POM.

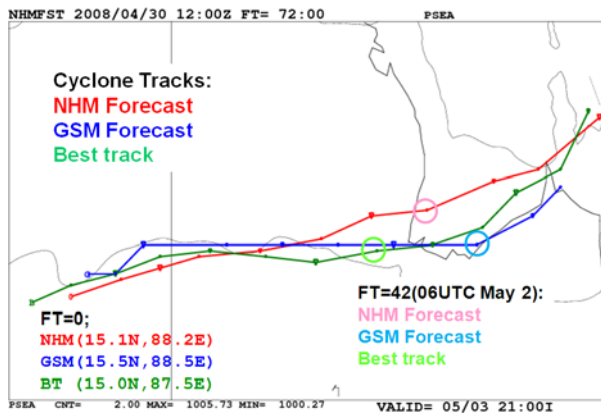


Fig. 2. Best track of Nargis and tracks predicted by NHM and GSM. Points enclosed with circles represent locations of the cyclone center at 06 UTC 2 May (FT=42).

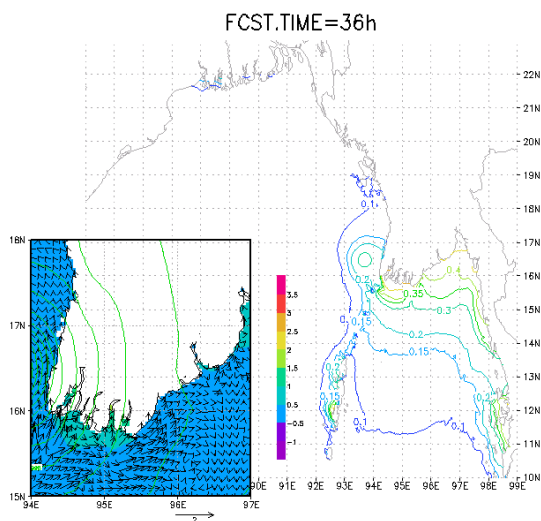


Fig. 3. Displacement of sea surface level simulated by POM at 00 UTC 2 May 2008 (FT=36). Lower left panel shows the enlarged view of sea level pressure (contour) and sea surface current (arrows).

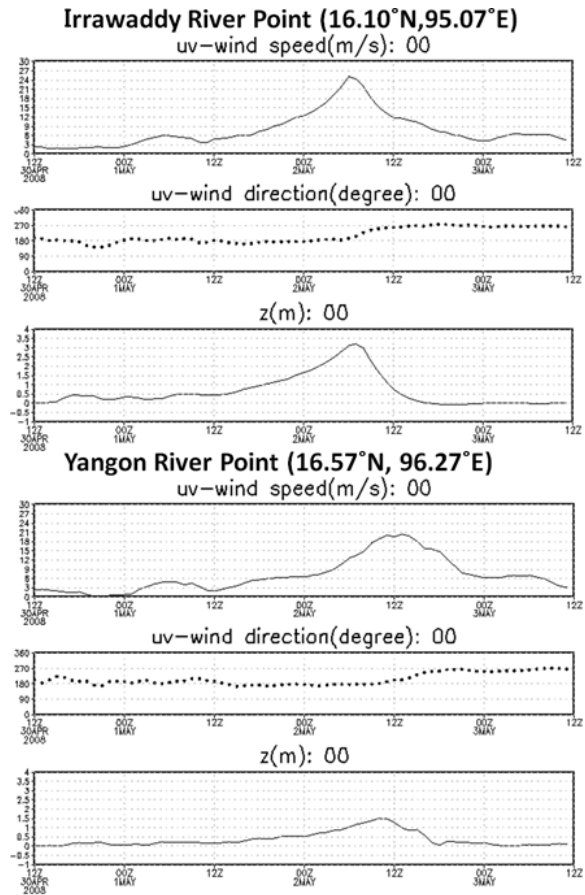


Fig. 4. Time sequence of surface (10 m) wind speed (upper) and wind direction (middle) given by NHM forecast, and water displacement of sea surface level simulated by POM (bottom) at the mouths of Irrawaddy River and Yangon River. Horizontal axes represent time window from 12UTC 30 Apr. to 12UTC 3 May. Value ranges of vertical axes are [0, 30] (m/s, wind speed), [0, 360] (degrees, wind direction) and [-1, 4] (m, water level).

An examination of the quality of a new snow parameterization scheme combined with the COSMO's land surface scheme TERRA

Ekaterina E. Machulskaya

Hydrometcenter of Russia, Moscow, Russia,
km@ufn.ru <http://meteoinfo.ru>

A validation study performed for COSMO's land surface one-dimensional scheme TERRA in stand-alone long-term regime exerted some deficiencies in the representation of snow water-equivalent depth (SWE) when compared with the observational data collected at the meteorological stations in Russia (Valdai, 1966-1983) and Germany (Lindenberg-Falkenberg, 2005-2006). Too high snow melting rates in spring lead to earlier dates of the snow complete ablation compared with observations and as consequence to earlier rise of the surface temperature above freezing point which begins immediately after snow ablation.

A new, more physically based parameterization of snow is suggested and implemented into TERRA. As the main component, this multilayered scheme includes description of the water phase transitions within snowpack. This scheme contains also description of the diffusive heat conduction through snowpack, simple radiative transport (extinction law), percolation of liquid water and semi-empirical parameterization of metamorphosis and compaction of snow.

The results, i.e., SWE and dates of the snow ablation obtained by TERRA with the new snow parameterization scheme are in closer agreement with the measurements then obtained with the control one (see Fig. 1). This effect is especially clear during those springs when there was no precipitation, since snowfall events in spring could mask too fast snowmelt that the default TERRA's more simple snow model shows. These experiments have shown that for the accurate representation of snow cover evolution it is necessarily to account for liquid water within snowpack and the possibility for liquid water to undergo repeated cycles of diurnal melting and night-time refreezing. It is worth to mention that the analytical calculation of snow density in the new scheme instead of its empirical calculation in the reference scheme leads to more realistic values of snow density (see Fig. 2) and, as a consequence, to more accurate values of geometrical snow heights (see Fig. 3).

Additional experiments with the same input data were performed in order to analyze the sensitivity of the TERRA with the control and new snow schemes to other parameterizations, for example to the parameterizations of snow albedo or snow cover fraction. These dependencies are of particular importance since they induce the snow-albedo feedback. The experiments have shown that 1) by means of only replacement of these dependencies it is impossible in many cases to improve the simulation of snow melting rates and 2) more physically based snow scheme reveals more sensitivity to perturbations of the parameters of abovementioned parameterizations.

Snow melting speed in turn determines hydrological outflow regime. Observational runoff data at Valdai shows that the spring flood in most years falls on April. The default snow scheme simulates the spring flood in March and underestimates the amount of it. The new snow scheme essentially improves the simulated runoff and in the experiments with new snow scheme the spring flood falls on April.

The study was supported by the Russian Foundation for Basic Research (Project no. 07-05-13566-ofi_ts).

Figure 1. Time series of snow water-equivalent depths at Valdai: observed (green circles) and simulated by TERRA with the reference (blue line) and new (red line) snow scheme.

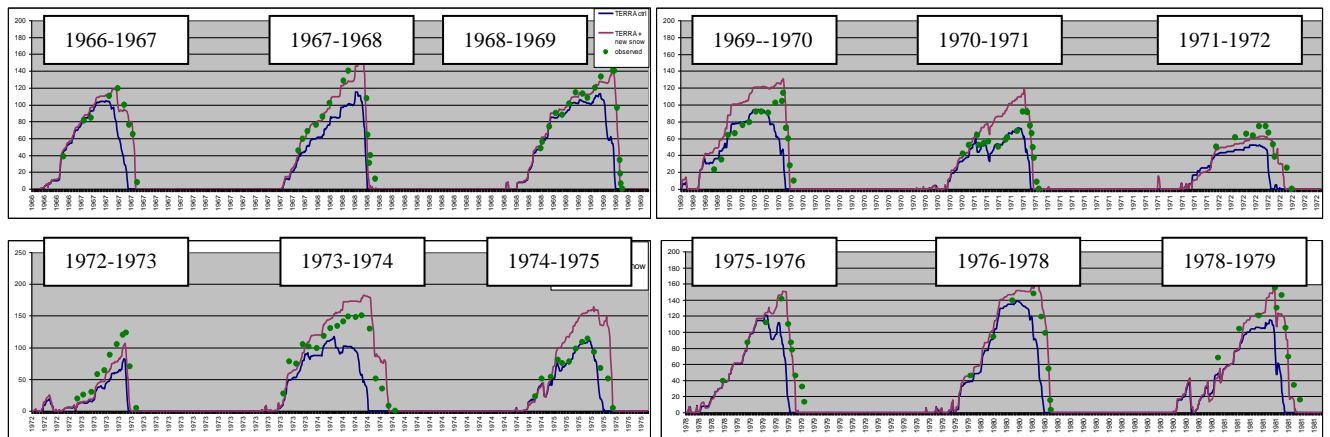


Figure 2. Time series of snow densities at Valdai, 1969-1975: observed (blue circles) and simulated by TERRA with the reference (yellow line) and new (red line) snow scheme.

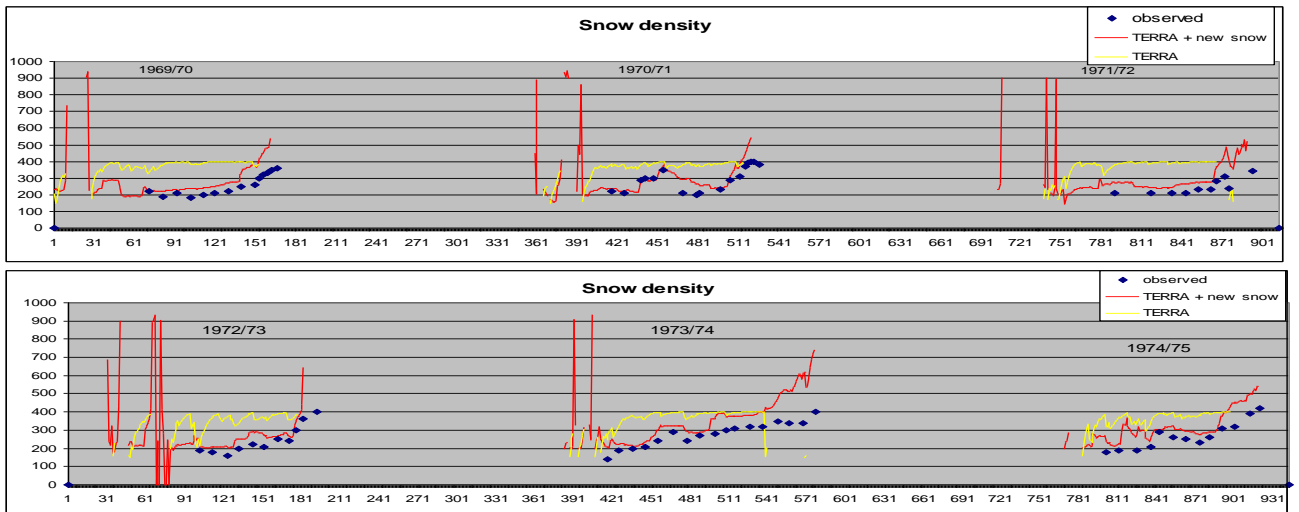
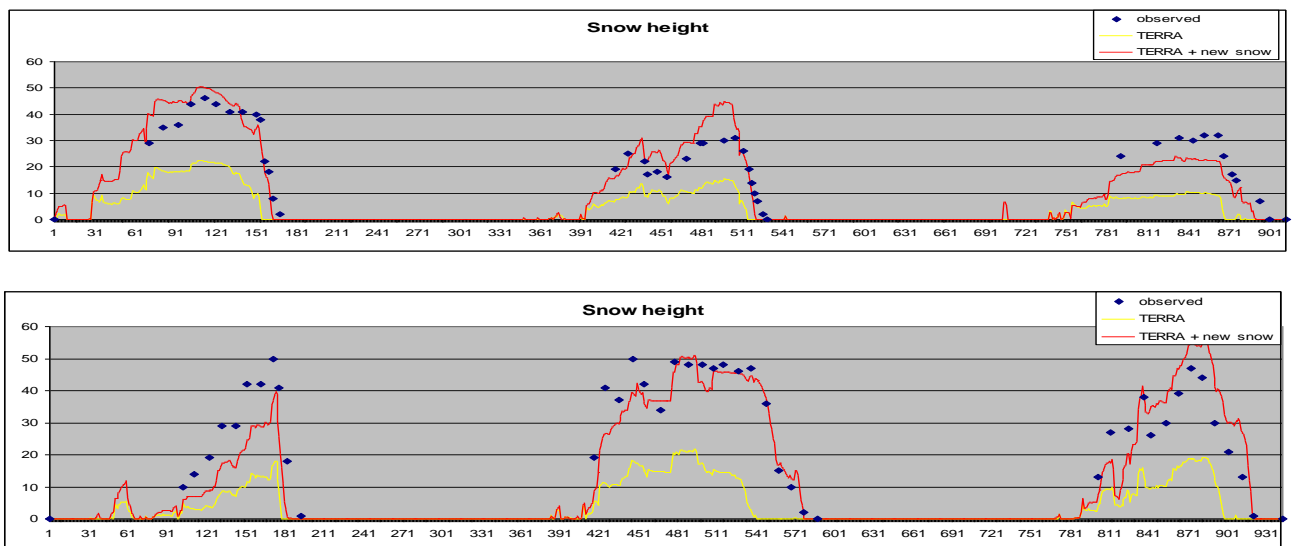


Figure 3. Time series of snow heights at Valdai, 1969-1975: observed (blue circles) and simulated by TERRA with the reference (yellow line) and new (red line) snow scheme.



EXPLOSIVE STORM DEVELOPMENT IN KERCH STRAIT: SIMULATION BY COSMO-RU MODEL AND SYNOPTIC ANALYSIS

Gdaly Rivin, Inna Rozinkina, Boris Peskov,
Anastasia Bundel, Tatyana Dmitrieva

Hydrometcenter of Russia, Moscow,

Ekaterina Kazakova
Moscow State University

Gdaly.Rivin@mecom.ru <http://meteoinfo.ru>

One of the most important cases considered was the storm over the Kerch Strait (between Black Sea and the Sea of Azov).

This report is devoted to the “case study” of a synoptic situation, definition of genesis of the phenomenon of intensive cyclone onset and of questions of adequacy of its reproduction in COSMO-RU model (Rivin, Rozinkina, 2009).

On November, 11th, 2007 in northern part of the Black sea there was a strong storm (speed of a wind reached 35 m/c). As a result in Kerch strait (between Azov and Black seas) 5 ships have sunk passage, were human victims, there was a catastrophic flood of oil.

This storm was created by a cyclone that has previously arisen over the Mediterranean sea and sharply became much more active within the Black sea (this situation looks like as “explosion”).

On figs 1 -8 some results of this case study are given.

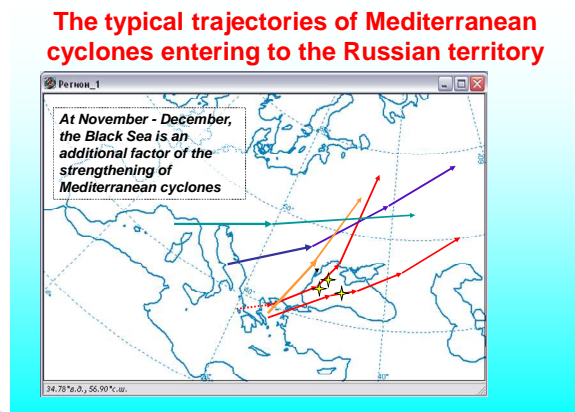


Fig. 1.

24-h forecast and reanalysis

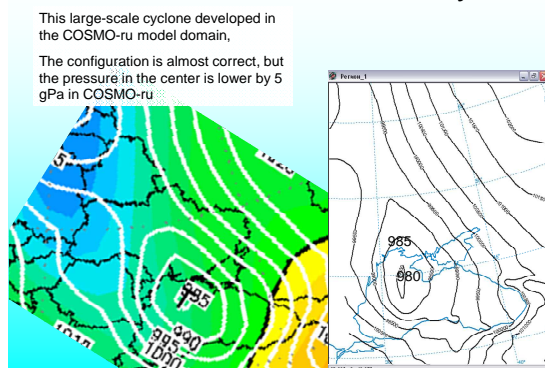


Fig. 3.

The storm in the Kerch Strait may be created only by very strong wind with strict direction as in the figure below

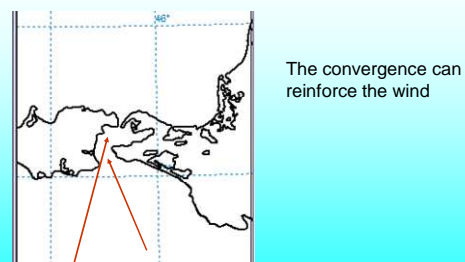


Fig. 4.

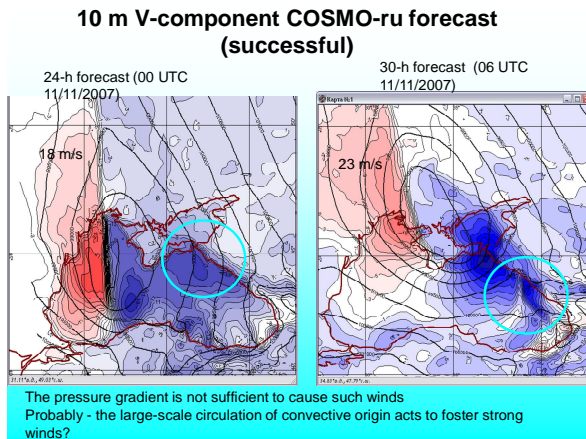


Fig. 5.

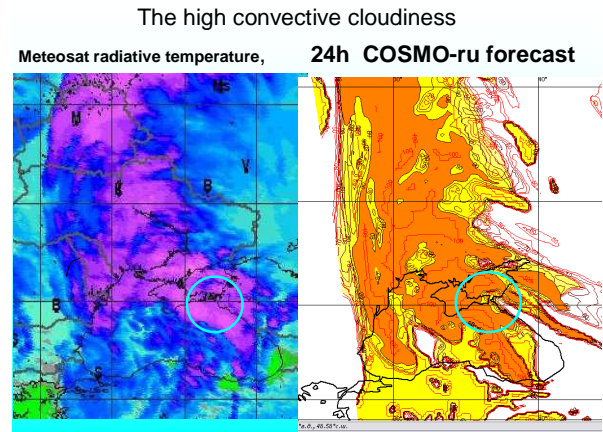


Fig. 6.

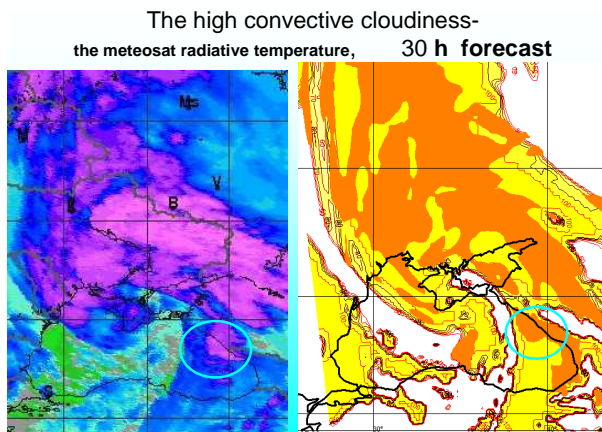


Fig. 7.

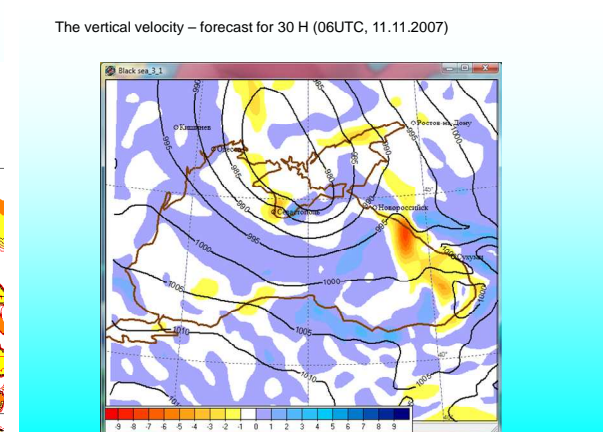


Fig. 8.

Conclusions

- The COSMO-RU forecasts of the 10-m wind velocity fields determined the storm in the Kerch Strait on November 11, 2007.
- The origin of strong wind was:
 - pressure gradients in the cyclone,
 - movements before fast-moving front,
 - vertical convective circulation,
 - convergence of movements of different types in the Kerch Strait gorge.
- COSMO-RU successfully simulated the configuration of high powerful clouds;
- COSMO-RU slightly underestimated velocity of the cyclone front movement and a small error in the cyclone depth.

Acknowledgements

The study was supported by the Russian Foundation for Basic Research (projects no. 07-05-13566-ofi_ts, 07-05-13607-ofi_ts).

References

Rivin G., Rozinkina I. (2009). The first steps of operational running of non-hydrostatic mesoscale model atmosphere COSMO-RU. Research Activities in Atmospheric and Oceanic Modelling, CAS/JSC WGNE, WMO (see this issue).

THE FIRST STEPS OF OPERATIONAL RUNNING OF NON-HYDROSTATIC MESOSCALE MODEL ATMOSPHERE COSMO-RU

Gdaly Rivin, Inna Rozinkina

Hydrometcenter of Russia, Moscow, Russia,
Gdaly.Rivin@mecom.ru <http://meteoinfo.ru>

The Consortium for Small-scale Modeling (COSMO, <http://www.cosmo-model.org/>) was formed in October 1998. Its general goal is to develop, improve and maintain a non-hydrostatic limited-area atmospheric model COSMO, to be used both for operational and for research applications by the members of the consortium.

In September 2007 Federal Hydrometeorology and Environmental Monitoring Service of Russia has entered to consortium COSMO for joint development and using mesoscale model COSMO with members of a consortium (services Germany, Greece, Italy, Poland, Romania and Switzerland).

The configuration COSMO-RU (40 levels, rotated system coordinate with rotated north pole with geographical latitude 35° and longitude 215° , territory of the European part of Russia: grid spacing 0.125° (14 km) with 168×300 grid points, time step 80 s) of model COSMO (version 4.3) is chosen and adapted to computing systems on the basis of Intel 64-bit processors Xeon and Itanium processors not only for preparation for planned reception in 2008-2009 of the super computer, but also realization of daily 78 h forecasts for territory of the European part of Russia.

For demonstration of an opportunity of the forecast of the dangerous phenomena with the help of model COSMO-RU the forecast of storm in Kerch strait on the data for 10.11.2007.00 is carried out. The analysis which has shown high efficiency of model COSMO-RU is spent.

Mesoscale model COSMO-RU with the grid step of 14 km is adapted to the weather technological line of the Hydrometeorological centre of Russia and release of forecasts meteorological elements on 78 h on the European territory of Russia in a quasi-operative mode on the current initial data and conditions on borders is organized two times in day (00 and 12 hours UTC) on 1 node (2 processors Xeon 5345, 2.33GHz, with 4 cores each and 32 Gb operative memory on node, 64-bit, OS - RHEL5 (Red Hat Enterprise Linux 5), Intel C++ 10.0.26, Intel Fortran 10.0.26, Intel MPI 3.0). For these forecasts the HMC of Russia receives by *ftp* GME data from DWD and produces the forecasts for 78 h for the European part of Russia. Time of the run with 8 cores (1 x 8 - topology) is 3h 35 min. Examples of skill of T_{2m} forecasts for different cities of Russia (26.07.2008-13.08.2008) see on fig.1.

Are carried out adaptation mesoscale model COSMO-RU to removed (taking place on territory of USA) computing system ALISA and numerical experiments (with use up to 256 cores) for a choice of optimum cartesian topology for model COSMO-RU on a basis 78 h of forecasts at the choice of effective decomposition of area of the forecast for minimization of time of the account with the help of package MPI. Similar work is spent for 448 cores of the new super computer ALTIX 4700 of Federal Hydrometeorology and Environmental Monitoring Service given in an experimental mode. Time of the run with 448 cores (14 x 32 - topology) is $267 \text{ s} = 4 \text{ min } 27 \text{ s}$. The estimation of the received acceleration speaks about high quality of the parallel algorithm, used in models COSMO-RU.

It raises confidence on fast development of opportunities of the new super computer of Federal Hydrometeorology and Environmental Monitoring Service for preparation and to application in an operative mode of system COSMO-RU for grids for almost whole Europe with steps of 7 km and for direct modeling deep convection with grid step of 2.8 km.

Acknowledgements

The authors thanks many of our colleagues from Roshydromet, German weather service and Intel for the great number of consultations, help, and patience, especially R. Vilfand, V. Antsyovich, Yu. Alferov, S. Lubov, A. Nedachina (Roshydromet), U. Schaettler, M. Gertz (German weather service), A. Naraikin, P. Shelepugin, M. Shutov (Intel) and E.Kazakova (Moscow state university).

The study was supported by the Russian Foundation for Basic Research (projects no. 07-05-13566-ofi_ts, 07-05-13607-ofi_ts).

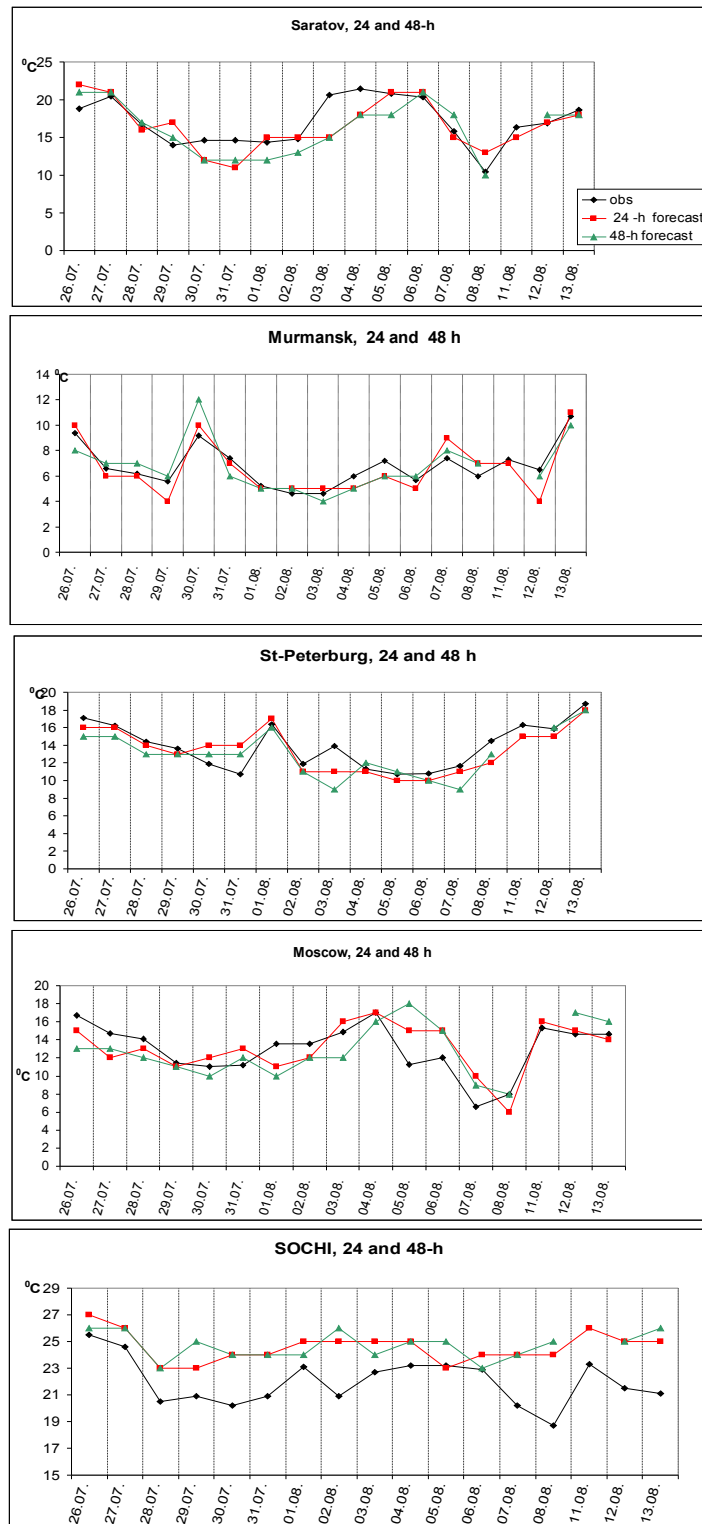


Fig.1. Examples of skill of T_{2m} forecasts for different cities of Russia (26.07.2008-13.08.2008)

Development of MRI/JMA mesoscale EPS at the WWRP Beijing Olympic Research and Development Project (B08RDP)

Kazuo Saito*, Masaru Kunii*, Masahiro Hara*, Hiromu Seko*,
Tabito Hara** and Munehiko Yamaguchi**

* Meteorological Research Institute, Tsukuba, Ibaraki 305-0052, Japan; ksaito@mri-jma.go.jp

** Numerical Prediction Division, Japan Meteorological Agency

The WWRP Beijing Olympic 2008 Forecast Demonstration / Research and Development Project (B08FDP/RDP) is an international research project for a short range forecast of the WMO World Weather Research Programme (WWRP), which succeeds the Sydney 2000FDP. The B08FDP/RDP is divided into two components; the FDP component for a very short range forecast up to 6 hours based on the nowcasting, and the RDP component for a short range forecast up to 36 hours based on the mesoscale ensemble prediction system (MEPS). Aims of the RDP project are to improve understanding of the high-resolution probabilistic prediction processes through numerical experimentation and to share experiences in the development of the real-time MEP system.

In 2008, the B08RDP experiment was conducted from 24 July to 24 August by six participants; the Meteorological Research Institute (MRI), NCEP, Meteorological Service of Canada (MSC), Austrian Zentral Anstalt fur Meteorologie und Geodynamik (ZAMG), National Meteorological Center of the China Meteorological Administration (NMC/CMA) and the Chinese Academy of Meteorological Sciences of CMA (CAMS/CMA). Intercomparisons of 36 hour EPS forecasts were conducted, and the forecast products were uploaded on the website of the B08RDP (<http://www.b08rdp.org>) in near real time.

MRI has developed a mesoscale ensemble prediction system collaborating with the Numerical Prediction Division of JMA. JMA nonhydrostatic model (NHM) was adopted as the forecast model. To ameliorate underestimations of convective rains and maximum temperatures in abnormally hot days found in the 2007 experiment (Saito et al., 2008a), tunings of model parameters for physical processes (K-F scheme and surface wetness) were done. As for initial condition, the JMA mesoscale 4D-var system was applied to Beijing area, assimilating rain gauge observations and precipitation analysis conducted in B08FDP project (Kunii et al., 2008).

As for initial perturbation methods, following five methods, i) Downscale of JMA one-week EPS (WEP), ii) Targeted global Singular vector (GSV), iii) Mesoscale Singular Vector (MSV), iv) Mesoscale BGM (MBD), v) Ensemble transform (LET) based on NHM-LETKF (Miyoshi and Aranami, 2006), were developed.

Lateral boundary perturbation methods were developed, where perturbations from the global ensemble prediction are added as the increment to

lateral boundary conditions given by the JMA's high resolution global forecast. The global ensemble prediction was initiated with the Global singular vectors for GSV, while the JMA one-week EPS was adopted for other 4 methods (WEP, MSV, MBD and LET) according to Saito et al (2008b).

Prior to the 2008 experiment, performance of above methods were verified by checking the ensemble spreads and the root mean square errors (RMSEs) of ensemble mean. Figure 1 shows time evolution of ensemble spreads of surface variables for 3-4 July 2008. Spreads by GSV are largest after FT=18, while in MSV, spread of surface precipitation grows most rapidly at first 6 hours. Spread of LET is relatively small and growth was slow. Figure 2 shows RMSEs of control run and the ensemble means by five methods at FT=24 for surface variables against analysis. RMSEs of ensemble means are smaller than control run except surface pressure by LET and WEP. RMSEs of GSV is the smallest, and MSV and MBD are the second best. Figure 3 shows the area of ROC. GSV is best for weak rains less than 3mm, while MBD and MSV are suitable for moderate or intense rain. The reason is likely that GSV tends to perturb synoptic scale disturbances while MBD and MSV tend to perturb mesoscale disturbances which are relate to local intense rains.

Considering above results, we selected GSV as the initial perturbation method at B08RDP experiment in 2008. Specifications of the mesoscale ensemble prediction system of MRI/JMA are listed in Table 1. Preliminary validations have shown the good performance of the MRI/JMA's mesoscale ensemble system.

References

- Kunii, M., K. Saito and H. Seko, 2008: Assimilation of Precipitation Data in Beijing Area. *CAS/JSC WGNE Research Activities in Atmospheric and Oceanic Modelling*, **37**, 1.15-1.16.
- Saito, K., H. Seko, M. Kunii and M. Hara, 2008a: Mesoscale Ensemble Prediction experiment for WWRP Beijing Olympic 2008 RDP --2007 preliminary experiment--. *CAS/JSC WGNE Research Activities in Atmospheric and Oceanic Modelling*, **37**, 1.23-1.24.
- Saito, K., M. Kunii, H. Seko, M. Yamaguchi and K. Aranami, 2008b: Implementation of lateral boundary perturbations into mesoscale EPS. *CAS/JSC WGNE Research Activities in Atmospheric and Oceanic Modelling*, **37**, 3.11-3.12.

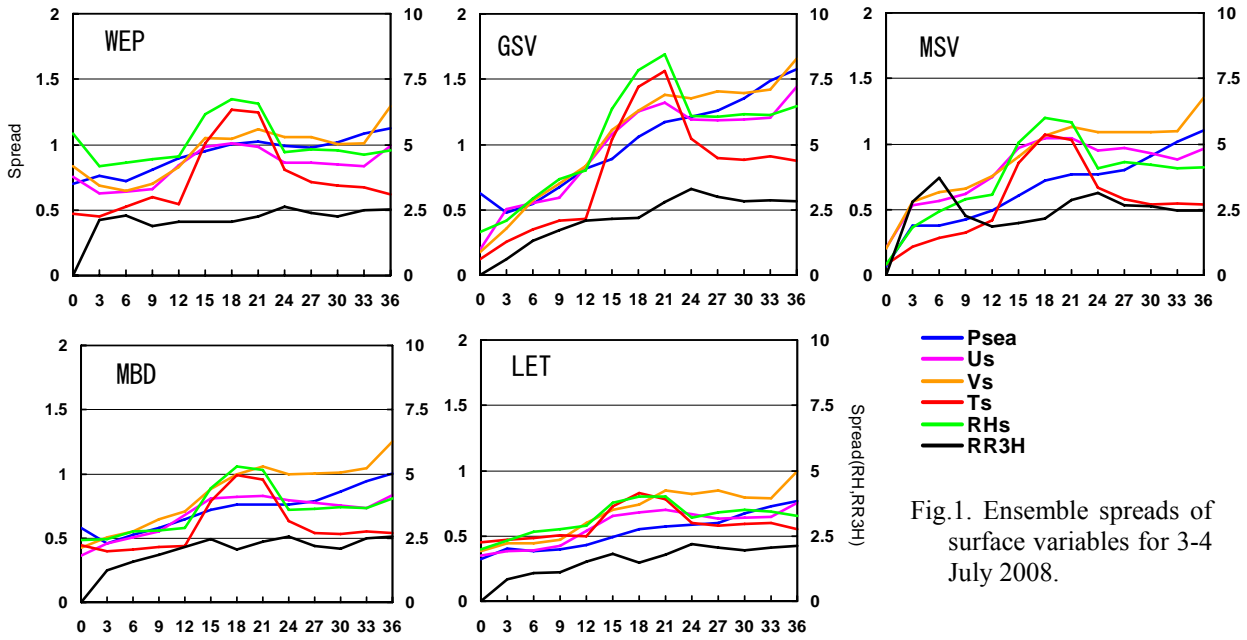


Fig.1. Ensemble spreads of surface variables for 3-4 July 2008.

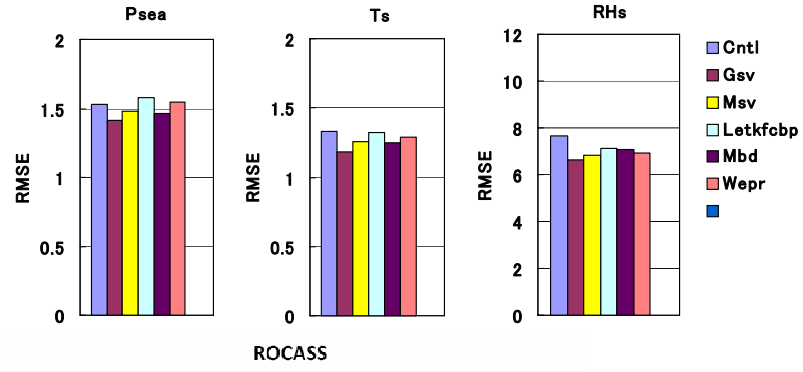


Fig. 2. RMSEs of surface variables against analysis for 3-4 July 2008.

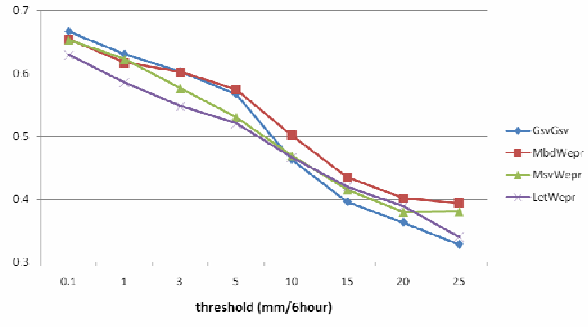


Fig. 3. Area of ROC against 6 hour precipitation intensity for 3-4 July 2008.

Table 1. Specifications of the B08RDP MEP system of MRI/JMA.

	2006 Experiment	2007 Experiment	2008 Experiment
Forecast model	NHM as of March 2006	NHM as of May 2007	NHM as of August 2008
Horizontal grid	221×201 ($\Delta x = 15\text{km}$)	232×200 ($\Delta x = 15\text{km}$),	No change
Vertical grid	Terrain-following coordinates, 40 levels	No changes	Generalized hybrid coordinates
Number of members	11 members	No changes	No changes
Initial condition	JMA operational regional 4D-Var analysis	No changes	Meso 4DVAR analysis for Beijing area
Initial perturbation	JMA one-week global EPS (TL159)	Targeted moist global SV (T63L40)	Targeted moist global SV (T63L40) (modified)
Lateral boundary	JMA RSM forecast (no perturbation)	No changes	JMA GSM forecast (20km L60)
Soil temperatures	4 layer prognostic soil temperatures	Initial perturbations are added	No changes

Influence of lateral boundary perturbations on the mesoscale EPS using BGM and LETKF

Kazuo Saito*, Hiromu Seko*, Masaru Kunii*, Masahiro Hara* and Takemasa Miyoshi **

* Meteorological Research Institute, Tsukuba, Ibaraki 305-0052, Japan, ** Maryland University
ksaito@mri-jma.go.jp

The Meteorological Research Institute (MRI) has been developing mesoscale ensemble prediction systems, collaborating with the Numerical Prediction Division of JMA. The development was also performed as a link of the WWRP Beijing Olympic 2008 Research and Development Project (B08RDP). In the B08RDP project, five initial perturbation methods were developed, including a mesoscale breeding growing mode (BGM) method and a method which employs the local ensemble transform Kalman filter (LETKF). In this report development of above two initial perturbation methods based on the mesoscale model and influence of lateral boundary perturbations on the mesoscale EPS are presented.

A mesoscale BGM method based on the JMA nonhydrostatic model (NHM) was developed by Saito et al. (2007; WGNE research activity report), where the magnitude of the bred perturbations, was evaluated by the moist total energy norm by Barkmeijer et al. (2001):

$$TE = \frac{1}{2} \iint \{ (U_p - U_C)^2 + (V_p - V_C)^2 \} + \{ \frac{c_p}{\Theta} (\theta_p - \theta_C)^2 \} + w_q \frac{L^2}{c_p \Theta} (q_p - q_C)^2 dS dP + \frac{1}{2} \int \{ \frac{R\Theta}{P_r} (P_{seaP} - \theta_{seaC})^2 \} dS.$$

Here, $\Theta=300K$, $Pr=800hPa$, $w_q=0.1$. In this study, following modifications have been added:

1) Horizontal resolution of NHM in the breeding cycle was set 15 km and normalized bred vectors were added as the increment to the initial condition of the 15 km EPS.

2) In normalization, the total energy norm was computed below 5.3 km and the normalization factor was defined by the square root of the ratio to the norm computed by statistical analysis errors in the JMA mesoscale analysis. 80 % of following values were adopted; PS: 0.6 hPa, U, V: 1.8 m/s*(Kg/m3), θ : 0.7 K, RH: 10 %.

3) In all breeding cycles, saturation adjustment was applied to the perturbed fields in the hybrid model plane.

Lateral boundary perturbations are given by an incremental method which uses perturbations from the JMA one-week global EPS. Perturbations are interpolated in time and space to 3 hourly lateral boundary conditions of NHM following Saito et al. (2008; WGNE research activity report).

Figure 1 shows time the evolution of ensemble spreads in the B08RDP verification area (30N-45N, 115E-125E) by the BGM method. Initial seed of the breeding was given by the JMA one-week EPS at 12 UTC of 2 July 2008, and 6 hourly 2 day breeding

cycles with a horizontal resolution of 40 km were conducted to obtain the initial perturbation increment at 12 UTC of 4 July. Without the lateral perturbation (Fig. 1a), growth of the ensemble spread is slow and reach the limit after FT=24. When the lateral perturbation was implemented in the forecast, ensemble spreads in the later half of the forecast period become larger (Fig. 1b) while the growth of spreads in the initial stage is not large. Figure 1c shows ensemble spreads when the lateral boundary perturbations were implemented in breeding cycles. Ensemble spreads become larger from the early stage of the forecast, and continue to increase throughout the forecast period. Spread of the surface temperature becomes largest in the day time (FT=12-21), corresponding to the diurnal change.

Figure 2 shows distribution of ensemble spread of temperature at 850 hPa level. Without the lateral boundary perturbation in breeding cycle (Fig.2a), initial spread is confined to small areas around the disturbance in China.

Figure 3 indicates RMS errors of ensemble means at FT=24 against the initial condition. RMSEs become smallest if the lateral boundary perturbation is implemented for both breeding cycles and the ensemble forecast.

Similar experiments were applied to the initial perturbation method using LETKF. Here, ensemble transform in NHM-LETKF (Miyoshi and Aranami, 2006; SOLA) were applied to create initial perturbations. Forecast analysis cycle is 6 hourly and horizontal resolution is 40 km as in the BGM method.

Figure 4 shows the time evolution of ensemble spreads by the LETKF method. Similar tendencies with the BGM method are seen; if the lateral boundary perturbation is omitted in the forecast analysis cycles (Fig.4a), the growth of spreads in the initial stage is not large. When the lateral boundary perturbations are implemented in the forecast analysis cycles (Fig. 4b), ensemble spreads become larger and continue to increase throughout the forecast period. The diurnal change become more distinct, however, the amplitude is smaller than that of BGM.

Distribution of initial perturbation (Fig. 5) is similar to that of BGM. If the lateral boundary perturbations are not implemented in the forecast analysis cycles (Fig. 5a), spreads near lateral boundary are small, which suggests the underestimation of the forecast error. Spreads over East China and Japan are smaller than BGM method corresponding to the observation density. This means that the magnitude of initial ensemble spreads in the LETKF method reflects the

analysis error. However, this advantage of the LETKF method to the BGM method was unclear in the statistical scores such as the RMSE of ensemble mean. Localization and sampling errors may affect the synoptic structure in the initial perturbation in the LETKF method.

Reference

Saito, K., M. Kunii, H. Seko, M. Yamaguchi and K. Aranami, 2008: Implementation of lateral boundary perturbations into mesoscale EPS. CAS/JSC WGNE Research Activities in Atmospheric and Oceanic Modelling, 37, 3.11-3.12.

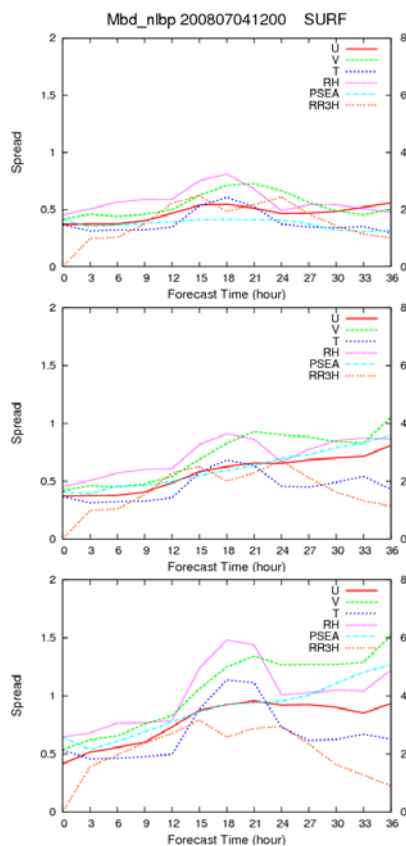


Fig. 1. Time evolution of the 11 member ensemble spreads of surface elements in the B08RDP verification area by the BGM method. Initial time is 4 July 2008. a) Without the lateral boundary perturbations. b) Lateral boundary perturbations only for the forecast. c) Lateral boundary perturbations for both in breeding cycles and the forecast.

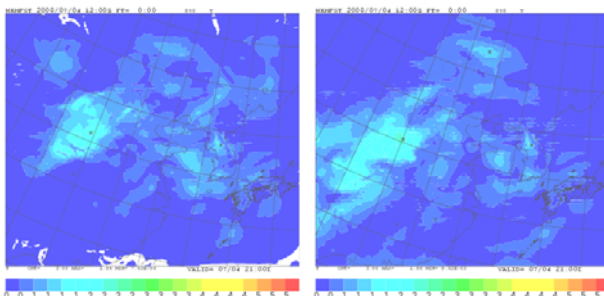


Fig. 2. Initial ensemble spread of the temperature at 850 hPa level. a) Lateral boundary perturbations only for the forecast. b) Lateral boundary perturbations for both in

breeding cycles and the forecast.

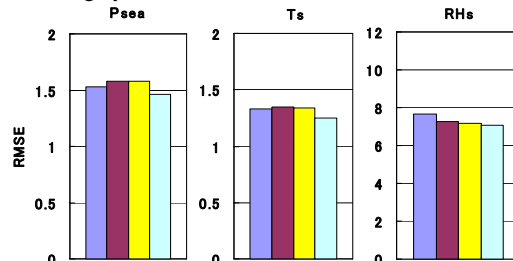


Fig. 3. RMS errors of ensemble means at FT=24 against the initial condition. (analysis at 12 UTC on the day after). Average of 3-4 July 2008. Blue: control, Brown: without lateral boundary perturbations, Yellow: Lateral boundary perturbations only for forecast. Light blue: Lateral boundary perturbations for both in breeding cycles and the forecast.

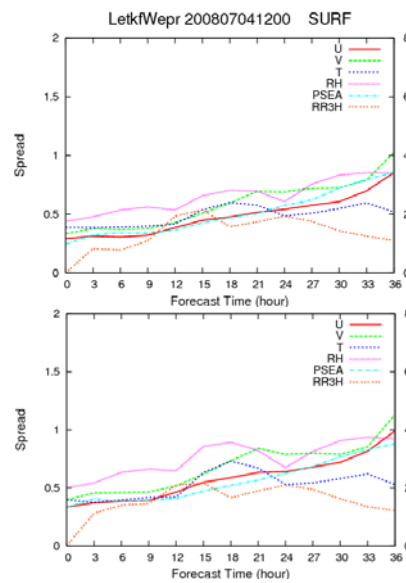


Fig. 4. Same as in Fig. 1b and 1c, except for the LETKF method.

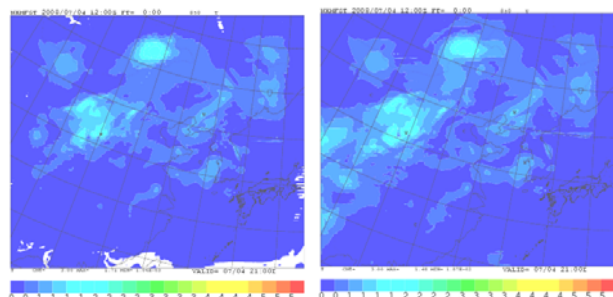


Fig. 5. Same as in Fig. 2, except for the LETKF method.

Ensemble Forecast Experiment of Cyclone Nargis

Kazuo Saito, Tohru Kuroda and Masaru Kunii

Meteorological Research Institute, Tsukuba, Ibaraki 305-0052, Japan; ksaito@mri-jma.go.jp

On 2 May 2008, cyclone Nargis made landfall in southwestern part of Myanmar and caused the worst natural disaster in the country which claimed more than one hundred thousand people by storm surge. This cyclone formed in the Bay of Bengal on 27 April and moved eastward while developing rapidly. Numerical simulations of Nargis and the associated storm surge have been performed by Kuroda et al (2009). Storm surge about 3.5 m was simulated in their study despite a positional lag of the cyclone center of about 150 km. It is well known that magnitude of storm surge highly depends on the track and intensity of the tropical cyclone and the numerical weather prediction has inevitable forecast errors due to uncertainties of initial/boundary conditions and model dynamics/physics. Considering the destructive disasters caused by storm surge, the warning and measures should be issued and taken respectively preparing for the worst case scenarios. The ensemble forecast may present realistic spread of tropical cyclone tracks while current most ensemble prediction systems (EPS) for typhoon forecast are based on global models and their horizontal resolutions are not enough to simulate local storm surge. In this study, we conducted a mesoscale ensemble forecast of cyclone Nargis using a mesoscale model with a horizontal resolution of 10 km, and examined spread of simulated tide levels.

A mesoscale EPS is developed to consider forecast errors in the storm surge forecast of cyclone Nargis. NHM with a horizontal resolution of 10 km is employed as the forecast model, which covers the Bay of Bengal and its surrounding areas by 341x 341 grid points. Hybrid-vertical coordinates with 40 stretched levels are used whose lowest level is located at 20 m AGL. These specifications are identical to the forecast experiment of Kuroda et al. (2009), and their simulation is adopted as the control run. Thus, JMA's high-resolution operational analysis at 12 UTC 30 April 2008 and the 6 hourly GSM forecast are used as the initial and boundary conditions of the control run. Initial and boundary perturbations are given by JMA's operational one-week EPS. Although the JMA's one-week EPS is conducted with a T213 (60km) L60 GSM, only 12 hourly low resolution (1.25 degrees) pressure plane (10 levels) forecast GPVs are available at MRI (and even at JMA) as the archived data. Incremental perturbations are extracted by subtracting the control run forecast from the first 10 positive ensemble members of JMA's one-week EPS, and are interpolated with time and space to the 6 hourly 10 km L40 initial and lateral boundary conditions for NHM. Since the highest level of the pressure plane forecast GPV is located at 200 hPa level and is lower

than the model top of NHM (22 km), perturbations at highest 8 levels of NHM are extrapolated from the incremental perturbation at 32nd level assuming the perturbation becomes zero at the model top. Adding 10 negative members, 20 mesoscale ensemble perturbations are prepared in all, and the saturation adjustment is applied to all initial and lateral boundary conditions.

Figure 1a compares predicted tracks of Nargis by the control run and member p01 and m01 with the best track. Track of member m01 is predicted in south of the control run and closer to best track while member p01 is predicted too northerly. Control run and both p01 and m01 are all predicted in east of best track, which means these runs predicted the landfall time too early. Main reason of this discrepancy is attributable to the positional lag in initial condition of control run at FT=0. Figure 1b shows predicted tracks until FT=42 by all ensemble members. The center positions of Nargis are distributed in an elliptic area with 200-300 km distant from the control run. This spread of predicted positions is roughly comparable to the statistical errors of JMA's typhoon track forecast in northwestern Pacific at FT=48. The major axis of the ellipse is oriented along the direction of cyclone's movement, suggesting that Nargis's forecast was a case where timing of landfall was relatively difficult. Predicted positions of the cyclone center in member p02, m05, m09 and p10 were better than the control run, while the intensities were weaker than the control run. The predicted center pressures were between 972 and 985 hPa. Here, we show forecasts by member m01 and p02 in Fig. 2.

Storm surge simulation is performed using surface wind forecasts by the mesoscale EPS. The Princeton Ocean Model (POM) is used with same specifications as in Kuroda et al.

Figure 3 shows time sequence of wind speeds, wind directions and tide levels predicted by all ensemble members at Irrawaddy (16.10N, 95.07E) and Yangon (16.57N, 96.27E) point. Wind speeds in some members have sharp minima in 2 May, corresponding to passage of the cyclone's 'eye'. At Irrawaddy point, tow members predict high tide levels near 4 m, while the timings are different from the control run. At Yangon point, where only moderate surge of 1.5 m was simulated in the control run, the maximum tide level reaches about 2.5 m. From the plume figures shown in Fig.3, we can compute the maximum, minimum and center magnitudes of tide levels with 25 % and 75 % probability values (Fig. 4). This result suggests that relying only on a single deterministic forecast is often dangerous. Quantitative information on forecast errors and reliability based on

the ensemble prediction are very important for effective risk management, and will become indispensable in the future disaster mitigation system.

Acknowledgment

We thank Nadao Kohno of JMA for their helps to run POM.

References

Kuroda, T., K. Saito, M. Kunii and N. Kohno, 2009: Numerical Experiments of Myanmar Cyclone Nargis. *CAS/JSC WGNE Research Activities in Atmospheric and Oceanic Modelling*. **39**. (this volume)

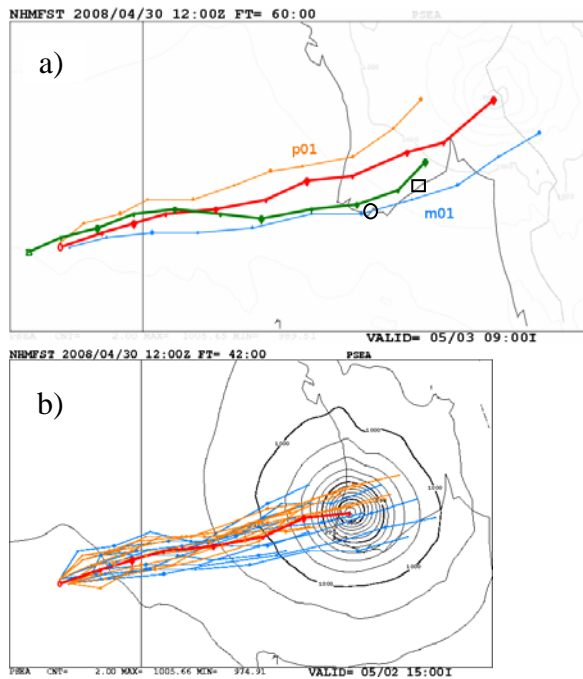


Fig. 1. a) Predicted tracks of Nargis until FT=60 (valid time 00 UTC 3 May 2008) by the control run (thick line) and the member p01 and m01. Corresponding best track is also indicated. Circle and square shows location of Irrawaddy and Yangon point, respectively. b) Predicted tracks until FT=42 (valid time 06 UTC 2 May 2008) by the control run (thick line) and the ensemble prediction.

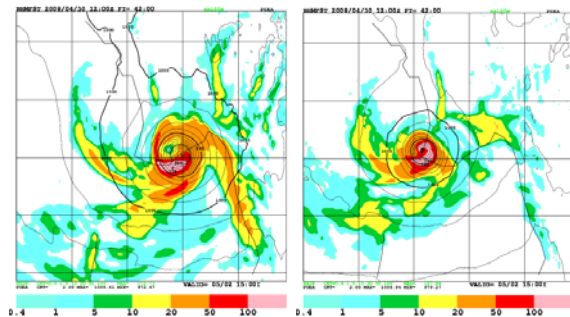


Fig. 2. Mean sea level pressure and 3 hour accumulated precipitation at FT=42 predicted by member m01 (left) and p02 (right).

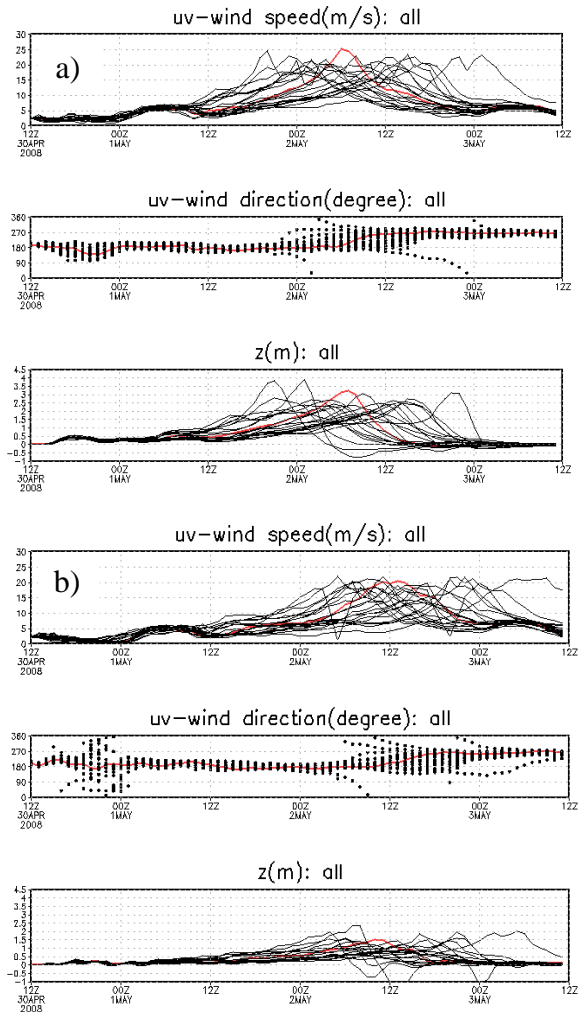


Fig. 3. a) Time sequence of wind speeds (upper), wind directions (middle) and tide levels (bottom) by all ensemble members at Irrawaddy point. b) Same as in a) but at Yangon point.

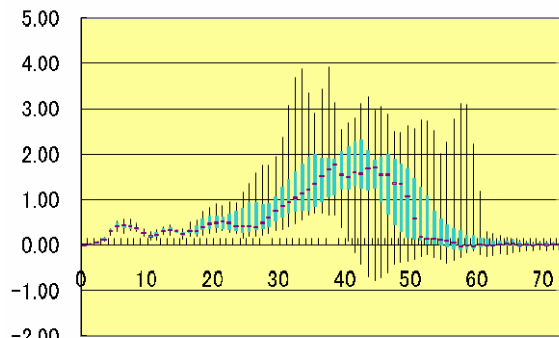


Fig. 4. Time sequence of the maximum, minimum and center magnitudes of tide levels at Irrawaddy point. Widths between 25 % and 75 % probability values are depicted with solid rectangles.

Implementation & progress of the AROME 2.5km modelling system at Météo-France

Yann Seity, Pierre Brousseau, Gwenaëlle Hello and François Bouttier
CNRM/GAME, Météo-France and CNRS
42 Av Coriolis, 31057 Toulouse France
francois.bouttier@meteo.fr

A new numerical weather prediction system has been implemented in operations at Météo-France in December 2008. It is called AROME (Applications of Research to Operations at Mesoscale) and covers mainland France at a 2.5km horizontal resolution (see example on Figure 1).

The AROME (model and data assimilation) system is derived from ECMWF's IFS software [2], Météo-France's ARPEGE/ALADIN [1], contributions from the ALADIN consortium [3] and from the Méso-NH research community [4]. AROME includes a non-hydrostatic, spectral semi-Lagrangian dynamical core, physical parametrizations of cloud microphysics (5 prognostic condensate species), subgrid turbulence (vertical mixing using prognostic turbulent kinetic energy plus EDKF shallow convection scheme), radiation (multiband RRTM-FM scheme), surface processes (tiles for sea, ice, snow, soil, vegetation, towns, with canopy model), and a 3-hourly 3D-Var sequential data assimilation that processes a variety of in situ, satellite and radar data (see [5]).

Real time experimentation of AROME over the past two years has shown it to be a beneficial tool for the forecasters as a complement to other, larger scale models. When compared to its nearest competitor (the 10km ALADIN-France model and data assimilation), AROME is shown to improve most low-level objective scores, and to bring useful guidance on high impact weather such as heavy rain, convective events, fog, coastal and orographic effects. For instance, it was shown to improve the forecast location of a flooding rain event that extended beyond the usual Mediterranean catchment areas (Figure 2); to provide indication of a tornado-favourable environment on a small scale destructive wind event (Figure 3); to improve the mapping of areas affected by high winds in a synoptic scale storm event.

Current priorities for further improvement are:

- to fix excessive precipitation in strong rain events. One suspects an erroneous interaction between the non-hydrostatic dynamics and microphysics in grid-scale convective towers.
- to double the vertical resolution in the lower troposphere. This is expected to improve the prediction of fog and low, stratiform clouds.
- to better represent the effect of subgrid orography. Although mountain waves are thought to be correctly modelled, systematic wind biases near crests and valleys may be due to a missing effect of subgrid roughness and blocking.
- to improve the model upper boundary condition. As the AROME grid does not extend very high into the stratosphere, a numerical relaxation towards boundary conditions provided by a larger scale model is beneficial.
- tunings of the physics, e.g. the subgrid shallow convection scheme
- to introduce the assimilation of radar reflectivities (see [5]) AIRS and IASI radiances
- to implement a native surface data assimilation (current SST, ice and soil prognostic fields are taken from the ALADIN data assimilation, which causes inconsistencies).
- to improve the 3DVar structure functions
- (later) to extend the geographical domain

Besides, extensive testing of higher resolution AROME models have begun, including real-time production of 1-km resolution forecasts over the Alps during the Winter 2009 World Ski Championship (Val d'Isère), 500-m tests and implication in developments for assistance to Air Traffic Management (ATM) including demonstration runs near some major airports. Current research with AROME is focused on modelling and data assimilation in Mediterranean regions, in preparation for the oncoming Hymex field experiment [6].

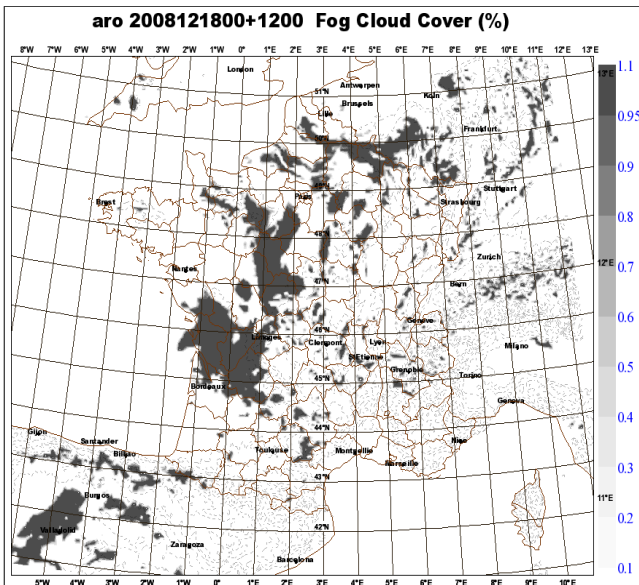


Figure 1: sample output from the first operational Arome forecast (fog field), showing the model domain.

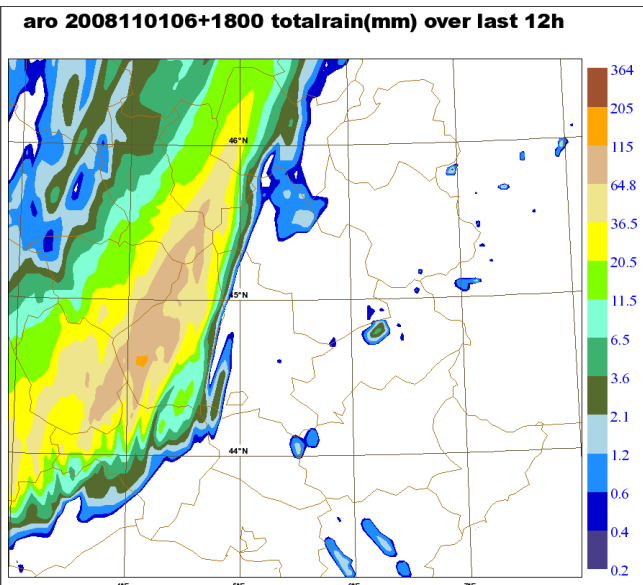


Figure 2: total rain forecast in the Lyons area (Gier flooding event). The area of maximum rain intensity is within 20km of the actual flooding event.

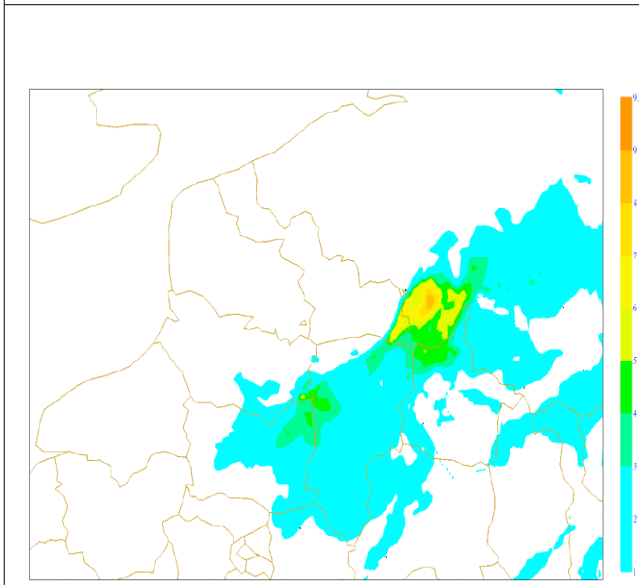


Figure 3: map of forecast SCP (supercell composite parameter) for a tornado event (Hautmont area, N of France, 8 Aug 2008) - the yellow area precisely matches the location of an observed tornado. Reproduced from [7]

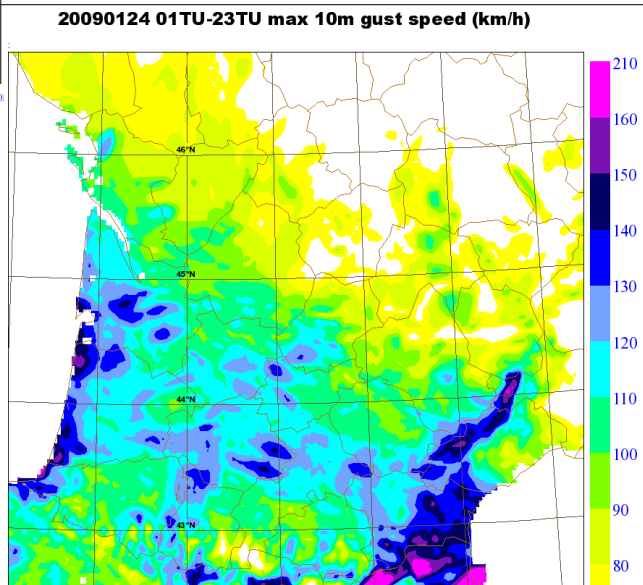


Figure 4: analysis of 10-m max gust speed for a day, combining Arome assimilated fields with in situ observations, during the 24 Jan 2009 storm over SW France.

References

- [1] <http://www.cnrm.meteo.fr/gmap/> and <http://www.cnrm.meteo.fr/arome/> : AROME system documentation, update bulletins and research papers.
- [2] <http://www.ecmwf.int/> is ECMWF's webpage with some documentation on the IFS
- [3] <http://www.cnrm.meteo.fr/aladin/> is the ALADIN consortium's official webpage
- [4] <http://mesonh.aero.obs-mip.fr/mesonh/> is the Méso-NH webpage with model documentation
- [5] Wattrelot, E. and T. Montmerle: Assimilation of radar data at convective scale at Météo-France. WGNE Blue Book 2009, in this volume.
- [6] <http://www.hymex.org/> is the webpage of the Hymex field experiment
- [7] Montmerle, T. and O. Nuissier, 2008: Les tornades en France, formation, climatologie, prévision. *Météo-France technical report.* (In French)

STRUCTURE OF THE REGIONAL HEAVY RAINFALL SYSTEM THAT OCCURRED IN MUMBAI, INDIA, ON 26 JULY 2005

Hiromu SEKO, Syugo HAYASHI, Masaru KUNII, and Kazuo SAITO

Email: hseko@mri-jma.go.jp

Forecast Research Department, Meteorological Research Institute, Tsukuba, Japan

1. Introduction

The heavy rainfall that occurred in Mumbai on 26 July 2005 produced the 24 hour rainfall amount exceeding 944.2 mm (Bohra et al, 2005). The rainfall at Santa Cruz, a suburb of Mumbai, started at 0600 UTC (11.5 India Standard Time (IST)) on 26 July 2005, and continued for 18 hours. The rainfall region observed by the TRMM satellite revealed that the horizontal scale of this rainfall event was several tens of kilometers. The airflow structure was investigated with the outputs of the Non-hydrostatic model with the horizontal grid interval of 1 km.

2. Design of experiment

This study used NHM with triple-nested grids (20 km, 5 km and 1 km). Initial and boundary conditions of 20km-NHM were obtained from the global analysis data of JMA. First, the analysis data at 11.5 IST (0600 UTC), 25 July were tested, but the heavy rainfall was not reproduced. Alternatively, the global analysis data at 5.5 IST (0000 UTC) 25 July were used as the initial condition of 20km-NHM. When this analysis was used as the initial data, an intense rainfall system was reproduced near Mumbai, though its generation time was 18 hours earlier than the observed one. In the satellite images of SSM/I, similarly developed convective systems existed on the western coast of India on 25 July, though their intensities were weaker than that of the heavy rainfall. Thus, we believe that the rainfall system simulated from this initial time had the information of the heavy rainfall. Outputs of 20km-NHM and 5km-NHM provided the initial and boundary conditions of 5km-NHM and 1km-NHM. The initial data of 5km-NHM and 1km-NHM were given by the outputs at the forecast time (FT) of 6 hours.

3. Evolution and structure of the simulated heavy rainfall

3.1 Evolution of the regional heavy rainfall (from FT=3-27 hours of 5km-NHM)

Evolution of the heavy rainfall was explained by the outputs of 5km-NHM. The rainfall regions were generated along the mountain range near the western coast of India by FT=3 (14.5 IST). An intense rainfall system was organized near Mumbai by FT=6 (17.5 IST). The system began to split into several rainfall cells along the mountain range at FT=18 (5.5 IST, 26 July), and then the intense rainfall was terminated at FT=23 (10.5 IST, 26 July). The rainfall amount in 17 hours from FT=6 to FT=23 caused by the system reached 1,149 mm. The rainfall amount and duration indicated that the heavy rainfall was quantitatively well-simulated.

3.2 Structure of the heavy rainfall system (at FT=6 hours of 1km-NHM)

Figure 1b depicts the rainwater mixing ratio of the regional rainfall system

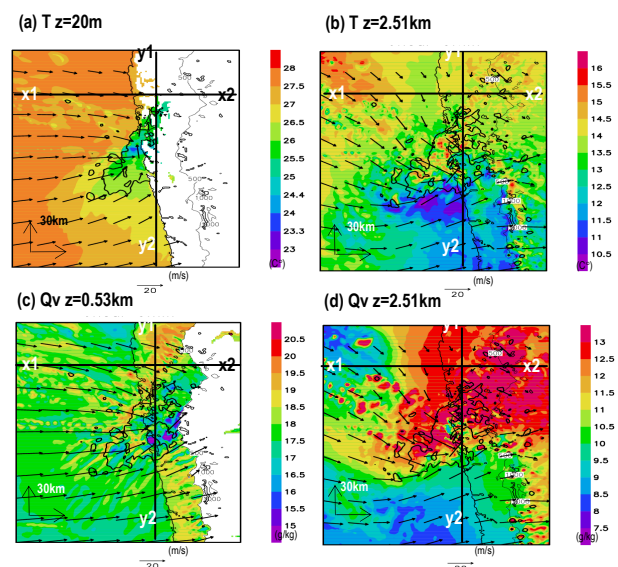


Fig. 1. Horizontal distribution of temperature (T) and water vapor mixing ratio (Qv) at FT=6 (23.5 IST) reproduced by 1km-NHM. Black contours indicate rainwater mixing ratio of 1 g/kg. Large arrows indicate the horizontal scale of 30 km.

reproduced by 1km-NHM. The intense rainfall system had already been organized by FT=6 (23.5 IST) 100 km south of Mumbai. The horizontal scale of regional heavy rainfall was several tens of kilometers.

The structure of heavy rainfall is revealed by the illustration of airflow (Fig. 2), and the distributions of temperature, water vapor and equivalent potential temperature (Figs. 1 and 3). The intense rainfall region extended southwestward from the mountain range near Mumbai. A cold pool developed between the intense rainfall region and the mountain range (Fig 1a, cold pool in Fig. 2). A westerly flow near the surface (Figs. 1a and 1c, A in Fig. 2) intruded the intense rainfall region from the west of the rainfall system, changing its moving direction to southeastward. This flow overrode the cold pool along the western side of the intense rainfall region (Fig. 1a). The westerly flow on the southern side of the system (Fig. 1a, E in Fig. 2) changed its moving direction to northeastward, and then passed the southern side of the system.

At the height of 0.53 km, the westerly flow from the west of the heavy rainfall (A in Fig. 2) was warmer and more humid than that in the westerly flow on the south of the system (E in Fig. 2). This warm humid westerly flow (A in Fig. 2) overrode the cold pool, and then produced an intense updraft at over 5 m/s at a height of 1.69 km (not shown). On the southern side of the intense rainfall region, a dry southwesterly flow occurred (Fig. 1c, head part of D in Fig.2). Figure 3a presents the vertical cross section of the equivalent potential temperature (θ_e) that crossed this dry flow region. The downdraft of low θ_e air, (dry airflow in Fig. 1c, head part of D in Fig. 2) occurred on the southern side of the system. This region extended northward as it descended, and then reached the lower layer (Fig. 3a). It was inferred that this descending dry airflow evaporated rain droplets and produced the cold downdraft.

At a height of 2.51 km, two key airflows were observed. The first one was a moist airflow that entered the rainfall system from the north (Fig. 2d, C in Fig. 2). This flow was expected to increase the rainfall amount because it provided water vapor to the rainfall system. Figure 3b depicts a vertical cross section of water vapor and vertical flux of water vapor along line x1-x2 in Fig. 1 where the humid westerly flow (B in Fig. 2) existed near the surface (Fig. 1c). Regions of upward water vapor flux exceeding $2 \times 10^{-3} \text{ kgm}^{-2}\text{s}^{-1}$, whose top reached a height of 3 km, occurred over the western slope and on the western side of the mountain range. This distribution indicated that the thick humid layer originated from the low-level humid airflow (B in Fig. 2) stagnated by the topography effect of the mountain range. The second key airflow was the relatively dry westerly flow that intruded into the southern side of the rainfall system (D in Fig. 2), where the downdraft was dominant. This dry airflow was cooled by the evaporation of the rain droplets, and then became the downdraft in the southern side of the rainfall system. This cold airflow enhanced the convective instability and produced the cold pool. Both airflows (C and D in Fig. 2) were favorable for maintaining the heavy rainfall.

References

Bohra, A. K., S. Basu, E. N. Rajagopal, G. R. Iyengar, M. D. Gupta, R. Ashrit, and B. Athiyaman, 2005: Heavy rainfall episode over Mumbai on 26th July 2005: Assessment of NWP Guidance, Report of NCMRWF, 25 pp.

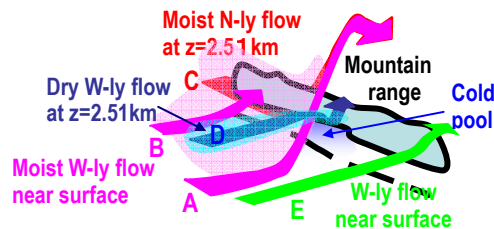


Fig. 2. Schematic illustration of the heavy rainfall.

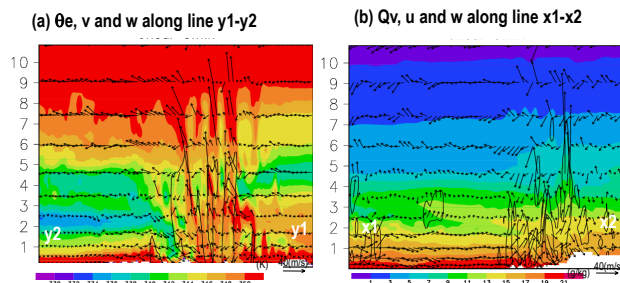


Fig. 3. Vertical cross sections of (a) equivalent potential temperature (θ_e) and (b) water vapor mixing ratio (Q_v) at FT=6 (23.5 IST) along the lines in Fig. 1. Vertical velocities in (a) and (b) are multiplied by 10 and 50, respectively. Contours in (a) and (b) show the region where rainwater mixing ratio exceeds 1 g/kg and where vertical flux of water vapor exceeds $2.0 \times 10^{-3} \text{ kgm}^{-2}\text{s}^{-1}$, respectively.

Operational Implementation of the Tephra Fall Forecast with the JMA Mesoscale Tracer Transport Model

Toshiki Shimbori^{*}, Yuri Aikawa[†] and Naoko Seino[‡]

^{*}*Volcanological Division, Japan Meteorological Agency, Tokyo 100-8122, Japan*

[†]*Numerical Prediction Division, Japan Meteorological Agency, Tokyo 100-8122, Japan*

[‡]*Meteorological Research Institute, Tsukuba, 305-0052, Japan*

The Japan Meteorological Agency (JMA) implemented the tephra fall forecast in Mar. 2008 as one of the forecasts on volcanic phenomena. This is a six-hour forecast of volcanic ash-fall areas, and is disseminated in graphical format when a large eruption occurs in Japan (e.g., if the height of the ash plume is greater than 3,000 m above the crater rim, or if the JMA volcanic alert level is higher than 3). The forecast is based on the outputs of the JMA Mesoscale Tracer Transport Model for volcanic ash. This model, which is based on the JMA Tracer Transport Model (Iwasaki et al., 1998), is applied to volcanic-ash forecasting with meteorological fields predicted by the operational JMA Mesoscale Model (MSM). Another application of the JMA Mesoscale Tracer Transport Model is the oxidant forecast (Takano et al., 2007).

A flowchart of the tephra fall prediction system is shown in Fig. 1. When an eruption occurs in a domestic volcano, we immediately obtain an observation report on the eruption describing the location, event time, plume height and so on. Based on this report and the assumed continuance of eruption, we create a model of an eruption column, which leads to the initial condition of the JMA Mesoscale Tracer Transport Model for volcanic ash. The model of the eruption column is composed of 100,000 tracer volcanic-ash particles with a grain size from about 100 μm to 0.001 mm and virtual mass. Then, these tracer particles are diffused from the eruption column during the continuance of eruption and transported with a time interval of three minutes using the hourly outputs of the MSM for the nearest initial time (00, 06, 12 or 18 UTC) to the event occurrence. In the model, the settling velocities of volcanic ash are considered (Suzuki, 1983). Finally, we count the number of deposited tracer particles per hour and transform their virtual mass into the surface density of ash-fall mass. The tephra fall forecast determines ash-fall areas as those with surface densities exceeding 0.1 g/m^2 .

The tephra fall forecast was activated for the eruptions that occurred at Sakurajima Volcano on 27 to 28 Jul. 2008 and at Asama Volcano on 1 Feb. 2009. The results are shown in Figs. 2 and 3, respectively. These forecasts were qualitatively good in comparison with the ash-fall observations. From a quantitative point of view, however, the predicted amounts of ash-fall were underestimated around the foot-level of the volcanoes. For quantitative tephra fall prediction, we will apply a high-resolution local forecast to the tracer transport model.

^{*} E-mail: shimbori@met.kishou.go.jp

References

- Iwasaki, T., T. Maki and K. Katayama, 1998: Tracer transport model at Japan Meteorological Agency and its application to the ETEX data. *JMA/NPD Tech. Rep.*, **35**, 33pp.
- Suzuki, T., 1983: A theoretical model for dispersion of tephra. *Arc Volcanism: Physics and Tectonics*. TERRAPUB, 95–113.
- Takano, I., Y. Aikawa and S. Gotoh, 2007: Improvement of photochemical oxidant information by applying transport model to oxidant forecast. *CAS/JSC WGNE Res. Activ. Atmos. Oceanic Modell.*, **37**, 0535-0536.

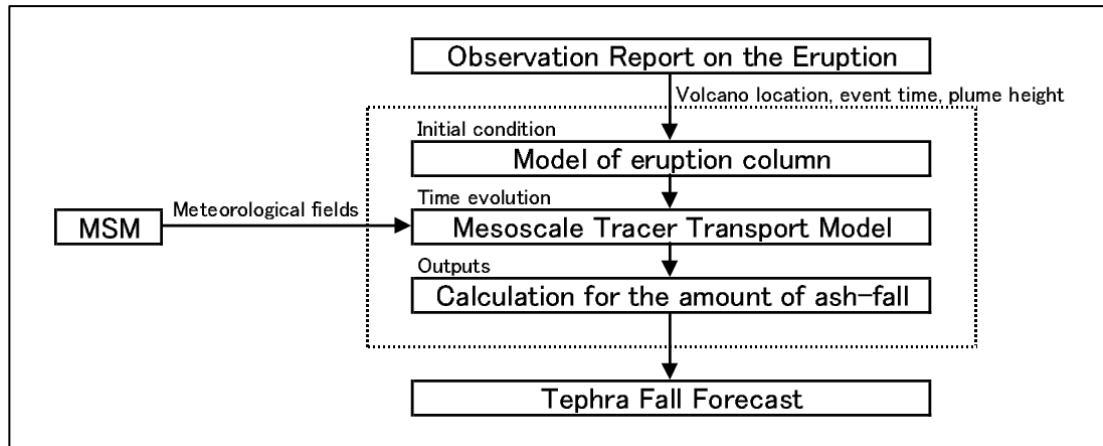


Fig. 1 Flowchart of the tephra fall prediction system

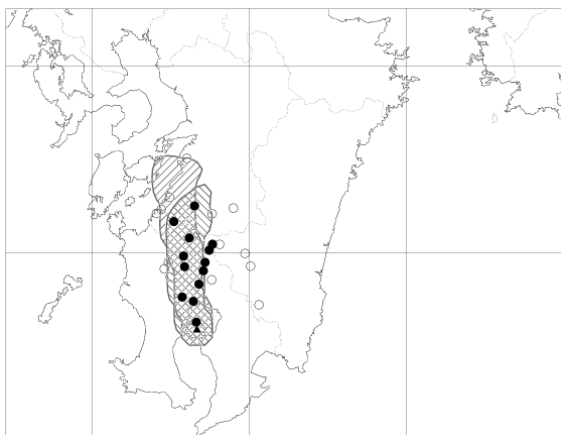


Fig. 2 Six-hour forecast of the two eruptions at Sakurajima Volcano (denoted by ▲) in Jul. 2008. 1st eruption (▨): from the event time at Jul. 27 22:05 UTC to the valid time at Jul. 28 04:00 UTC with a plume height of 3,300 m above the crater; 2nd eruption (●): from the event time at Jul. 28 01:10 UTC to the valid time at 07:00 UTC with a plume height of 3,200 m. In comparison with ash-fall observations (●: observed; ○: not observed).

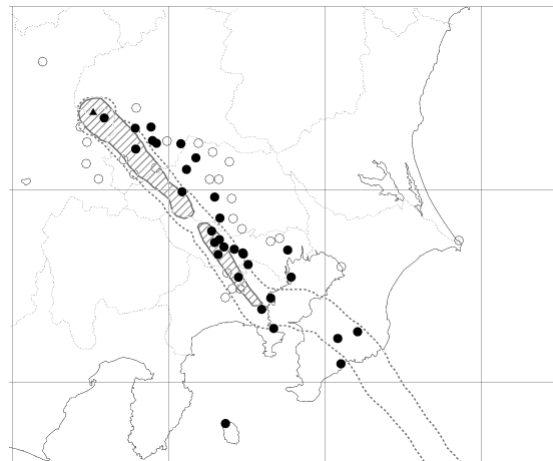


Fig. 3 Six-hour forecast of the eruption at Asama Volcano (denoted by ▲) on 1 Feb. 2009 from the event time at 16:51 UTC to the valid time at 23:00 UTC with a plume height of 2,000 m above the crater. In comparison with ash-fall observations (the notations are the same as those in Fig. 2). For reference, the dotted-line contour indicates 0.01 g/m^2 .

Asymmetric features of near-surface wind fields in typhoons revealed by the JMA mesoscale analysis data

Mitsuru Ueno and Masaru Kunii

Typhoon Research Department, Meteorological Research Institute

e-mail: mueno@mri-jma.go.jp

Recently the relationships between azimuthal wavenumber-one inner-core structures of tropical cyclones (TCs), and environmental vertical wind shear, have been increasingly investigated with numerical simulations at high resolution and theoretical considerations. However, due to the lack of detailed observations, which are usually obtained through a special field observational program, the results have not been endorsed by observational studies in a systematic manner. A viable alternative for detailed observations is analytical gridded data produced with a relatively high resolution by using a state-of-the-art data assimilation technique, such as the mesoscale analysis (hereafter referred to as "meso-analysis") data operationally produced at the Japan Meteorological Agency (JMA).

Over the years, researchers have developed parametric wind models to depict the surface winds within a TC. Parametric models have shown utility in creating wind fields as input to models such as the wave model, storm surge model, statistical-parametric model to predict TC wind radii, and pressure–wind model to relate the minimum central pressure to maximum surface winds in TCs. In most of such studies storm motion is assumed to be the only contributor to the near-surface wind asymmetry in TCs. Furthermore, most of previous theoretical studies on the wind distribution in the TC boundary layer have focused on the effect of TC translation on the wind distribution. Based on results from a real data simulation of Typhoon Chaba (2004), however, Ueno (2008) suggested that vertical wind shear could play a dominant role in determining the wind structure in the TC boundary layer insofar as the shear is significantly large. In the simulation low-level inflow tends to occur in the downshear-left quadrant, in accordance with the preferred location of rainfall maximum, and the strongest tangential wind is about 90° of azimuth downstream of the maximum inflow. A better knowledge of the role of vertical wind shear in determining the near-surface wind asymmetry would help to significantly improve parametric wind models.

The purpose of the present study is to document, in an extensive manner using the meso-analysis data, the influence of environmental vertical wind shear on the wavenumber-one asymmetries of near-surface wind components in the TC inner-core region. As a first step to quantify the shear contribution to the near-surface wind asymmetry in real TCs, here in the present study we analyze the wind fields at about 20 m height (the lowest analysis level) obtained from the JMA operational meso-analysis, putting emphasis on the azimuthal location of wind maximum and its relevance to shear and storm motion. For the purpose a total of 190 cases from 35 typhoons observed during 2004–2007 seasons are examined. Figure 1 shows the directional relationship between shear and tangential wind maximum. The azimuth of tangential wind maximum is found by performing the

first-order Fourier decomposition of earth-relative wind field with respect to the surface center. In the figure both the shear direction and azimuth of tangential wind maximum are defined relative to the direction of storm motion. The storm motion vector is calculated from the JMA best-track position fixes. As expected, and in accordance with various earlier observational studies, the wind maxima are found predominantly to the right of TC motion. Interestingly, however, a small fraction (17 %) of the total cases exhibit a left-of-motion maximum and it occurs only in cases in which the shear direction is nearly equal to the storm heading. This result is in qualitative agreement with expectations from the simplified formulae derived in Ueno and Kunii (2009), which predict the tangential wind maximum in storm-relative coordinates to the left of TC center facing in the direction of enhanced eyewall convection.

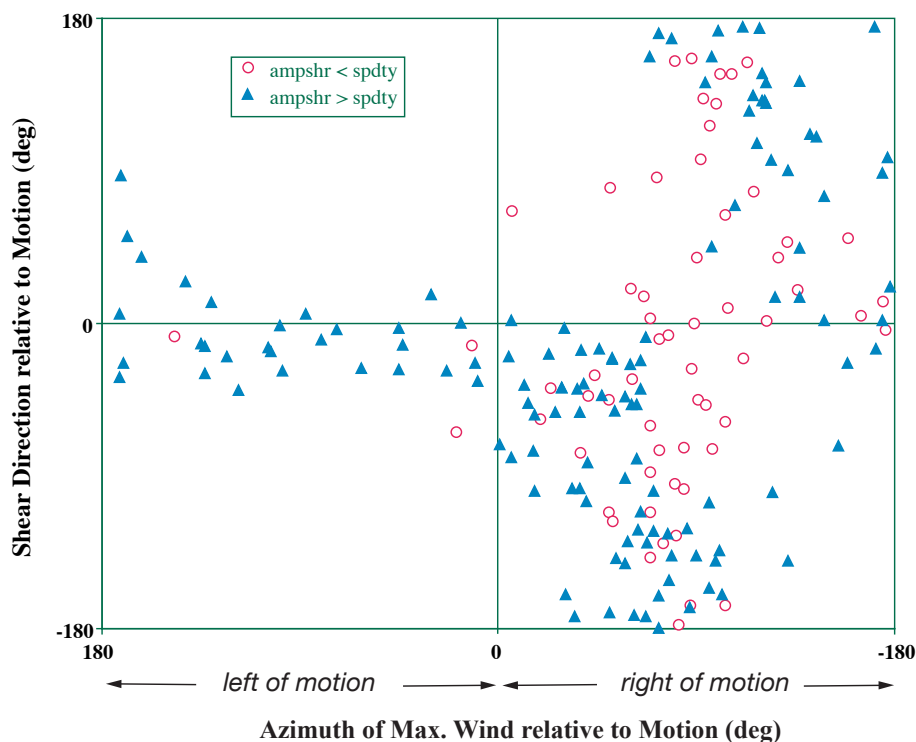


Figure 1: Directional relationship between vertical wind shear and tangential wind maximum. Vertical axis denotes the direction (in degree) of shear relative to that of storm motion vector with positive (negative) values for the shear to the left (right) of the motion, while horizontal one represents the azimuthal direction (in degree) of tangential wind maximum relative to storm heading. The sampled cases are stratified into two groups according to whether the shear magnitude is greater than storm translation speed (closed triangles) or not (open circles).

References

Ueno, M., 2008: Effects of ambient vertical wind shear on the inner-core asymmetries and vertical tilt of a simulated tropical cyclone. *J. Meteor. Soc. Japan.* **86**, 531-555.